The client-binding domain of the cochaperone SGTA/Sgt2 has a helical-hand structure that binds a short hydrophobic helix

(120 of 120)

Ku-Feng Lin, Michelle Fry*, Shyam Saladi*, and William M. Clemons, Jr.

* contributed equally to this work

Correspondence: W.M.C, clemons@caltech.edu
Division of Chemistry and Chemical Engineering, California Institute of Technology, Pasadena, California 91125

Keywords: Tail-anchored proteins, Protein targeting, co-chaperones, Ubiquilins, Sti1, Hop

Abstract (150 words – currently 149)

The correct targeting and insertion of tail-anchored (TA) integral membrane proteins (IMP) is critical for cellular homeostasis. The mammalian protein SGTA, and its fungal homolog Sgt2 (Sgt2/A), binds hydrophobic clients and is the entry point for targeting of ER-bound TA IMPs. Here we reveal molecular details that underlie the mechanism of Sgt2/A binding to TA clients. We establish that the Sgt2/A C-terminal region is conserved but flexible, sufficient for client binding, and has functional and structural similarity to the DP domains of Sti1. A molecular model for Sgt2/A-C reveals a helical hand forming a hydrophobic groove, consistent with a higher affinity for TA clients with hydrophobic faces and a minimal length of 11 residues. Finally, we show that a hydrophobic face metric improves the predictions for TA localization *in vivo*. The structure and binding mechanism positions Sgt2/A into a broader class of helical-hand domains that reversibly bind hydrophobic clients.

Introduction

An inherently complicated problem of cellular homeostasis is the biogenesis of hydrophobic IMPs which are synthesized in the cytoplasm and must be targeted and inserted into a lipid bilayer. Accounting for ~25% of transcribed genes [1], IMPs are primarily targeted by cellular signal binding factors that recognize a diverse set of hydrophobic alpha-helical signals as they emerge from the ribosome [2-4]. One important class of IMPs are tail-anchored (TA) proteins whose hydrophobic signals are their single helical transmembrane domain (TMD) located near the C-terminus and are targeted post-translationally to either the ER or mitochondria [5-9]. In the case of the canonical pathway for ER-destined TA IMPs, each is first recognized by homologs of mammalian SGTA (small glutamine tetratricopeptide repeat protein) [4,6,10,11]. Common to all signal binding factors is the need to recognize, bind, and then hand off a hydrophobic helix. How such factors can maintain specificity to a diverse set of hydrophobic clients that must subsequently be released remains an important question.

Homologs of the human SGTA and fungal Sgt2 (hereafter referred to as *Hs*SGTA for *Homo sapiens* and *Sc*Sgt2 fo*r Saccharomyces cerevisiae*, collectively Sgt2/A) are involved in a variety of cellular processes regarding the homeostasis of membrane proteins including the targeting of TA IMPs [9,12-14], retrograde transport of membrane proteins for ubiquitination and subsequent proteasomal degradation [15], and regulation of mislocalized membrane proteins (MLPs) [16,17]. Among these, the role of Sgt2/A in the primary pathways responsible for targeting TA clients to the endoplasmic reticulum (ER) are best characterized, *i.e.* the fungal Guided Entry of Tail-anchored proteins (GET) or the mammalian Transmembrane Recognition Complex (TRC) pathway. In the GET pathway, Sgt2 functions by binding a cytosolic TA client then transferring the TA to the ATPase chaperone Get3 (human TRC40) with the aid of the heteromeric Get4/Get5 complex (human TRC35/Ubl4A/Bag6 complex) [13,18-20]. In this process, TA binding to Sgt2, after hand-off from Hsp70, is proposed as the first committed step to ensure that ER, but not mitochondrial, TAs are delivered to the ER membrane [3,13,21]. Subsequent transfer of the TA from Sgt2 to the ATP bound Get3 induces conformational changes in Get3 that trigger ATP hydrolysis, releasing Get3 from Get4 and favoring binding of the Get3-TA complex to the Get1/2 (mammalian CAML/WRB) receptor at the ER leading to release of the TA into the membrane [22-26]. Deletions of GET genes (*i.e. get1*Δ, *get2*Δ, or *get3*Δ) cause cytosolic aggregation of TAs

62 dependent on Sgt2 [26,27].

63 In addition to targeting TA IMPs, SGTA may also promote degradation of IMPs through the
64 proteasome by cooperating with the Bag6 complex, a heterotrimer containing Bag6, TRC35, and
65 Ubl4A, which acts as a central hub for a diverse physiological network related to protein targeting
66 and quality control [19,28-30]. The Bag6 complex can associate with ER membrane-embedded
67 ubiquitin regulatory protein UbxD8, transmembrane protein gp78, proteasomal component
68 Rpn10c, and an E3 ubiquitin protein ligase RNF126 thereby connecting SGTA to ER associated
69 degradation (ERAD) and proteasomal activity. Depletion of SGTA significantly inhibits turnover
70 of ERAD IMP clients and elicits the unfolded protein response[16]. Furthermore, the cellular level
71 of MLPs in the cytoplasm could be maintained by co-expression with SGTA, which possibly
72 antagonize ubiquitination of MLPs to prevent proteasomal degradation [15,17]. These studies
73 demonstrate an active role of SGTA in triaging membrane proteins in the cytoplasm and the breadth
74 of SGTA clients including TAs, ERAD clients, and MLPs all harboring one or more TMD. SGTA
75 roles in disease have been linked to polyomavirus infection [31], neurodegenerative disease
76 [27,32], hormone-regulated carcinogenesis [33,34], and myogenesis [35], although the underlying
77 molecular mechanisms are still unclear.

78 The architecture of Sgt2/A includes three structurally independent domains that define the
79 three different interactions of Sgt2/A (Fig 1A) [12,36-39]_ENREF_19. The N-terminal domain
80 forms a homo-dimer composed of a four-helix bundle with 2-fold symmetry that primarily binds
81 to the ubiquitin-like domain (UBL) of Get5/Ubl4A for TA targeting [36,40] or interacts with the
82 UBL on the N-terminal region of BAG6 [41] where it is thought to initiate downstream degradation
83 processes [15,28,29]. The central region comprises a co-chaperone domain with three repeated
84 TPR motifs arranged in a right handed-superhelix forming a 'carboxylate clamp' for binding the
85 C-terminus of heat-shock proteins (HSP) [12,42]. The highly conserved TPR domain was
86 demonstrated to be critical in modulating propagation of yeast prions by recruiting HSP70 [27]
87 and may associate with the proteasomal factor Rpn13 to regulate MLPs [43]. More recently, it was
88 demonstrated that mutations to residues in the TPR domain which prevent Hsp70 binding impair
89 the loading of TA IMPs onto Sgt2 in yeast [21], consistent with a direct role of Hsp70 in TA IMP
90 targeting via the TPR domain. The C-terminal methionine-rich domain of Sgt2/A is responsible
91 for binding to hydrophobic clients such as TA IMPs [11,37,44]. Other hydrophobic segments have
92 been demonstrated to interact with the domain such as the membrane protein Vpu (viral protein U)

93 from human immunodeficiency virus type-1 (HIV1), the TMD of tetherin [44], the signal peptide
94 of myostatin [35], and the N-domain of the yeast prion forming protein Sup35 [27]. All of these
95 studies suggest that the C-terminus of Sgt2/A binds broadly to hydrophobic stretches, yet structural
96 and mechanistic information for client recognition is lacking.

97 In this study, we provide the first structural characterization of the C-domains from Sgt2/A
98 (Sgt2/A-C) and show that, in the absence of substrate, they are relatively unstructured. We
99 demonstrate a conserved region of the C-domain, defined here as C_{cons}, is sufficient for client
100 binding. Analysis of the C_{cons} sequence identifies six amphipathic helices whose hydrophobic
101 residues are crucial for client binding. Combining this with *ab initio* structure prediction and
102 biochemistry in total demonstrates that C_{cons} has structural homology to the client-binding domain
103 of the co-chaperone Sti1/Hop. Artificial TA clients are used to define the properties critical for
104 binding to Sgt2/A-C. We further show that these principles extend to the TA proteome and are
105 sufficient to properly categorize the cellular localization of TA clients. Finally, the combined
106 results lead to a mechanistic model where Sgt2/A-C falls into the broader class of helical-hand
107 containing proteins involved in the binding and release of hydrophobic alpha-helices.
108

109 ## Results

110 ### The flexible Sgt2/A-C domain

111 Based on sequence alignment (Fig. 1*A*), the C-domain of Sgt2/A contains a conserved core
112 of six predicted helices flanked by unstructured loops that vary in length and sequence. Previous
113 experimental work had suggested that this region was particularly flexible, as the domain in the
114 *Aspergillus fumigatus* was sensitive to proteolysis [12]. Similarly, for *Sc*Sgt2-TPR-C, the sites
115 sensitive to limited proteolysis primarily occur within the loops flanking the conserved helices
116 (Fig. 1*A, red arrows* and S1*B*). This flexible nature of the C-domain likely contributes to its
117 anomalous passage through a gel-filtration column where *Sc*Sgt2/A-C elutes much earlier than the
118 similarly-sized, but well-folded Sgt2/A TPR-domain (Fig. 1*B*). The circular dichroism (CD)
119 spectra for both homologs suggests that the C-domain largely assumes a random-coil conformation,
120 with 40-45% not assignable to a defined secondary structure category (Fig. 1*C*) [45]. This lack of
121 stable tertiary structure is further highlighted by the well-resolved, sharp, but narrowly dispersed
122 chemical shifts of the backbone amide protons in ^{1}H-^{15}N HSQC spectra of Sgt2/A-C (Fig. 1*D,E*),
123 indicating a significant degree of backbone mobility, similar to natively unfolded proteins [46] and

124 consistent with results seen by others [47]. The larger hydrodynamic radius matches previous
125 small-angle X-ray scattering measurement of the TPR-C protein that indicated a partial unfolded
126 characteristic in a Kratky plot analysis [12].
127
128 **The conserved region of the C-domain is sufficient for substrate binding**
129 Several lines of evidence suggest the conserved region of the C-domain binds substrates. First,
130 during purification the Sgt2-C-domain was cut at several specific sites (Fig. 1*A*). Proteolysis
131 occurred primarily in the poorly-conserved N-terminal region (between Asp_{235}-Gly_{258}) and at
132 Leu_{327}. This suggests that the intervening conserved region, Gly_{258} and Leu_{327} on *Sc*Sgt2 and its
133 corresponding region on *Hs*SGTA, may mediate TA client binding (Fig. 2*A, grey*). To test this,
134 various his-tagged Sgt2/A constructs were co-expressed with MBP-tagged TA client (Sbh1) and
135 binding was detected by the presence of captured TA by various Sgt2/A constructs bound to the
136 affinity resin (Fig 2*B*). As previously seen [13], we confirm that the Sgt2/A-TPR-C alone is
137 sufficient for capturing a TA client (Sbh1) (Fig. 2*B*). As one might expect, the C-domain was also
138 sufficient for binding the TA client. The central region of Sgt2/A-C contains six conserved helixes,
139 hereafter referred to as Sgt2/A-C_{cons}, and is sufficient for binding to the TMD of Sbh1 with an N-
140 terminal MBP-tag. For Sgt2, the minimal conserved region H1-H5 (ΔH0) poorly captures a TA
141 client, while in SGTA this minimal region is sufficient for capturing the client at a similar level as
142 the longer C_{cons} domain (Fig. 2*D*).
143 The six predicted helices in Sgt2/A-C_{cons} are amphipathic (Fig. 1*A* and Fig. 2*C*) suggesting
144 that they use the hydrophobic faces of the helices for binding to client. To probe this, each of these
145 helices was mutated to replace the larger hydrophobic residues with alanines dramatically reducing
146 the overall hydrophobicity. For all of the helices, alanine replacement of the hydrophobic residues
147 significantly reduces binding of Sbh1 to Sgt2/A (Fig. 2*E*). While these mutants expressed at similar
148 levels to the wild-type sequence, one cannot rule out that these changes do not broadly affect the
149 tertiary structure of this domain. In general, these results imply that these amphipathic helices are
150 directly involved in the interaction with client. The overall effect on binding by each helix is
151 different with mutations in the helices 1-3 having the most dramatic reduction in binding
152 suggesting that these are more crucial for TA complex formation. It is also worth noting, as this is
153 a general trend, that SGTA is more resistant to mutations that affect binding than Sgt2 which likely
154 represents different threshold requirements.

155

156 **Molecular modeling of Sgt2/A-C domain**

157 Despite the need for a molecular model, the C-domains have resisted structural studies, likely
158 due to the demonstrated inherent flexibility. With six conserved α-helical amphipathic segments
159 (Fig. 1*A*) containing hydrophobic residues critical for TA-client binding (Fig. 2*C,E),* we expect
160 some folded structure to exist. Therefore, we performed *ab initio* molecular modeling of Sgt2-C
161 using a variety of prediction methods [48-51] resulting in a diversity of putative structures. Of the
162 various models, only the highest scored structures from Quark [48] consistently result in a similar
163 tertiary fold (Fig. 3*A*). The general architecture contained a clear potential TA client binding site,
164 a hydrophobic groove formed by the amphipathic helices. The groove is approximately 15 Å long,
165 12 Å wide, and 10 Å deep, which is sufficient to accommodate three helical turns of an alpha-helix,
166 ~11 amino acids (Fig. 3*B*). For the prediction, while the entire C-domain was used, the N- and C-
167 termini of Sgt2 do not adopt similar structures across the various models consistent with their
168 expected higher flexibility (Fig. 3*C*).

169 To validate the model, we interrogated the accuracy of the predicted spatial location of the
170 helices by experimentally determining distance constraints from crosslinking experiments. Based
171 on the model, four pairs of residues in close spatial proximity and one pair far-apart were selected
172 and mutated to cysteines (Fig. 3*D*). In the experiment, an artificial TA client containing a cMyc-
173 tagged BRIL (small, 4-helix bundle protein [52]) with a C-terminal TMD consisting of eight
174 leucines and three alanines is co-expressed with Sgt2-TPR-C cysteine variants, purified, and then
175 oxidized to form disulfide crosslinks if the residues are near each other [53]. Crosslink formation
176 is identified by comparing the products after protease digestion where bond formation results in a
177 reducing-agent sensitive ~7.7 kDa fragment (Fig. 3*D*). For the wild-type (cysteine-free) sequence,
178 no higher molecular weight bands are observed at ~7.7kDa. For the N285/G329 pair which is too
179 distant for disulfide bond formation, no higher band is observed. For the remaining pairs that are
180 predicted to be close enough for bond formation, the 7.7kDa fragment is observed in each case
181 and is labile in reducing conditions. These results support the structures obtained in the Quark
182 derived C_{cons} model.

183

184 **Structural similarity of Sgt2/A-C domain to STI1 domains**

185 Attempts to glean functional insight for Sgt2/A-C from BLAST searches did not reliably

186 return other families or non Sgt2/A homologs making functional comparisons difficult. A more
187 extensive domain-based search using definitions from the similar modular architecture database
188 (SMART) [54] identified a similarity to domains in the yeast co-chaperone Sti1. First called DP1
189 and DP2 due to their prevalence of aspartates (D) and prolines (P), these domains have been shown
190 to be required for client-binding [55,56] and are termed 'STI1'-domains in bioinformatics
191 databases [54]. In yeast Sti1, and its human homolog Hop, each of the two STI1 domains (DP1
192 and DP2) are preceded by Hsp70/90-binding TPR domains, similar to the domain architecture of
193 Sgt2/A. Deletion of the second, C-terminal STI1-domain (DP2) from Sti1 *in vivo* is detrimental,
194 impairing native activity of the glucocorticoid receptor [55]. *In vitro*, removal of the DP2 domain
195 from Sti1 results in the loss of recruitment of the progesterone receptor to Hsp90 without
196 interfering in Sti1-Hsp90 binding [57]. These results implicate DP2 in binding of Sti1 clients. In
197 addition, others have noted that, broadly, STI1-domains may present a hydrophobic groove for
198 binding hydrophobic segments of a client [55,56]. Furthermore, the similar domain organizations
199 (*i.e.* Sgt2/A TPR-C, Sti1 TPR-STI1) and molecular roles could imply an evolutionary relationship
200 between these co-chaperones. Indeed, a multiple sequence alignment of the Sgt2-C_{cons} with several
201 yeast STI1 domains (Fig. 4*A*) reveals strong conservation of structural features. H1-H5 of the
202 predicted helical regions in the C_{cons} align directly with the structurally determined helices in the
203 DP2 domain of Sti1; this includes complete conservation of helix breaking prolines and close
204 alignment of hydrophobic residues defining amphipathic helices [55].
205 Based on the domain architecture and homology, we believe it is reasonable to make a direct
206 comparison between the STI1 domain and Sgt2/A-C_{cons}. A structure of DP2 solved by solution
207 NMR reveals that the five amphipathic helices assemble to form a flexible helical-hand with a
208 hydrophobic groove [55]. The lengths of the alpha helices in this structure concur with those
209 inferred from the alignment in Fig. 4*A*. Our molecular model of Sgt2-C_{cons} is strikingly similar to
210 this DP2 structure. An overlay of the DP2 structure and our molecular model in Fig. 4*C*
211 demonstrates both Sgt2-C_{cons} and DP2 have similar lengths and arrangements of their amphipathic
212 helices (Fig. 4*B,C* and Fig. S3). Consistent with our observations of flexibility in Sgt2/A-C_{cons},
213 Sti1-DP2 generates few long-range NOEs between its helices indicating that Sti1-DP2 also a
214 flexible architecture [55]. We consider this flexibility a feature of these helical-hands for reversible
215 and specific binding of a variety of clients.
216

217 **Binding mode of TA clients to Sgt2/A**

218 We examined the C_{cons} surface that putatively interacts with TA clients by constructing
219 hydrophobic-to-charge residue mutations that are expected to disrupt capture of TA clients by
220 Sgt2/A. Similar to the helix mutations in Figure 2, the capture assay was employed to establish the
221 relative effects of individual mutations. A baseline was established based on the amount of TA-
222 client Sbh1 captured by wild-type Sgt2/A-C. In each experiment, Sbh1 expresses at the same level;
223 therefore, differences in binding should directly reflect the affinity of Sgt2/A mutants for clients.
224 In all cases, groove mutations from hydrophobic to aspartate led to a reduction in TA client binding
225 (Fig. 5*A* and *B*). The effects are most dramatic in Sgt2 where each mutant significantly reduced
226 binding by 60% or more (Fig. 5*A*). While all SGTA individual mutants saw a significant loss in
227 binding, the results were subtler with the strongest being only ~36% (Fig. 5*B*). Double mutants
228 were stronger with a significant decrease in binding relative to the individual mutants, more
229 reflective of the individual mutants in Sgt2. As seen before (Fig. 2), we observe that mutations
230 toward the N-terminus of Sgt2/A-C have a stronger effect on binding than those later in the
231 sequence.

232

233 **Sgt2/A-C domain binds clients with a hydrophobic segment ≥ 11 residues**

234 With a molecular model for Sgt2/A-C_{cons} and multiple lines of evidence for a hydrophobic
235 groove, we sought to better understand the specific requirements for TMD binding. To probe this,
236 Sgt2/A-TPR-C complex binding with designed TA clients where a number of variables are tested
237 including the overall (sum) and average (mean) TMD hydrophobicity, length of the TMD, and the
238 distribution of hydrophobic character within a TMD. These artificial TMDs were constructed as
239 C-terminal fusions with the architecture cMyc-tag, cytoplasmic BRIL, a hydrophilic linker (Gly-
240 Ser-Ser), and the TMD (Leu/Ala helical stretch followed by a Trp) (Fig. 6*A*). The total and mean
241 hydrophobicity are controlled by varying the helix-length and Leu/Ala ratio (1.82/0.38 TM
242 tendency hydrophobicity values). For clarity, we define a syntax for the various artificial TA clients
243 to highlight the various properties under consideration: hydrophobicity, length, and distribution.
244 The generic notation is TMD-length[number of leucines] which is represented for example as
245 18[L6] for a TMD of 18 amino acids containing six leucines.

246 Our first goal with the artificial constructs was to define the minimal length for a TMD to
247 bind to the C-domain. As described earlier, capture of His-tagged Sgt2/A-TPR-C with the various

248 TA clients were performed. We define a relative binding efficiency as the ratio of captured TA
249 client by a Sgt2/A variant normalized to the ratio of a captured WT TA client by the same Sgt2/A
250 variant, in this case the model ER-bound Bos1. The client 18[L13] shows a comparable binding
251 efficiency to Sgt2/A-TPR-C as that of Bos1 (Fig. 6*B*). From the helical wheel diagram of the TMD
252 for Bos1, we noted that the hydrophobic residues align on one side of the helix. Therefore, we
253 optimized our various model clients to contain a 'hydrophobic face' while shortening the length
254 and maintaining the average hydrophobicity of 18[L13] (Fig. 6*B*). Shorter helices of 14 or 11
255 residues, 14[L10] and 11[L8], also bound with similar affinity to Bos1. Helices shorter than 11
256 residues, 9[L6] and 7[L5], were not able to bind Sgt2/A (Fig. 6*B*) establishing a minimal length of
257 11 residues for the helix consistent with the dimensions of the groove predicted for the structural
258 model (Fig. 3).
259 Since a detected binding event occurs with TMDs of at least 11 amino acids, we decided to
260 probe this limitation further. The dependency of client hydrophobicity was tested by measuring
261 complex formation of Sgt2/A and artificial TA clients containing an 11 amino acid TMD with
262 increasing number of leucines (11[Lx]). As shown in Fig. 6*C*, increasing the number of leucines
263 monotonically enhances complex formation, echoing previous results [58]. *Hs*SGTA binds to a
264 wider spectrum of hydrophobic clients than *Sc*Sgt2, which could mean it has a more permissive
265 hydrophobic binding groove as reflected by the milder impact of alanine replacement and Asp
266 mutations in SGTA-C to TA binding (Fig. 2*C* and Fig. 5*A*).
267
268 **Sgt2/A-C preferentially binds to TMDs with a hydrophobic face**
269 Next, we address the properties within the TMD of TA clients responsible for Sgt2/A binding.
270 In the case of Sgt2/A, it has been suggested that the co-chaperone binds to TMDs based on
271 hydrophobicity and helical propensity [58]. For the most part, varying the hydrophobicity of an
272 artificial TA client acts as expected, the more hydrophobic TMDs bind more efficiently to Sgt2/A
273 TPR-C domains (Fig. 6*C*). Our C_{cons} model suggest the hydrophobic groove of Sgt2/A-C protects
274 a TMD with highly hydrophobic residues clustered to one side (see Fig. 3*B*). Helical wheel
275 diagrams demonstrate the distribution of hydrophobic residues along the helix (*e.g.* bottom Fig.
276 6*D*). Testing various TMD pairs with the same hydrophobicity, but different distributions of
277 hydrophobic residues demonstrates TA clients with clustered leucines have a higher relative
278 binding efficiency than those with a more uniform distribution (Fig. 6*D*). The clustered leucines

279 on the TMDs create a hydrophobic face which potentially interacts with the hydrophobic groove
280 formed by the Sgt2/A-C_{cons} region, corresponding to the model in Fig. 3*B*.
281
282 **Organization of hydrophobic residues in probable client TMDs**
283 So far, the interpretation from the structure that Sgt2/A-C binding to clients via a hydrophobic
284 groove is supported by the binding preferences of Sgt2/A-TPR-C. As Sgt2/A is the entry point into
285 TA IMP targeting to the ER, we were interested in whether TMD hydrophobic faces were relevant
286 to sorting of TA clients in the cell. Previous results demonstrate that hydrophobicity is a dominant
287 factor in selection between the ER and mitochondria [59]; therefore, the reference yeast and human
288 genomes from UniProt [60] were screened for putative TA IMPs and filtered for unique genes
289 longer than 50 residues. Uniprot and TOPCONS2 [61] were used to identify genes that encoded
290 an IMP containing a single TMD within 30 amino acids of the C-terminus [62] and lacked a
291 predicted signal sequence (as determined by SignalP4.1 [63]) (Fig. 7*A* and Table S1). Based on
292 their UniProt-annotated localizations [60], TA IMPs are subcategorized as ER, mitochondrial,
293 peroxisomal, and unknown. While our set encompasses proteins previously predicted as TA IMPs
294 [64,65], it is larger and we believe a more accurate representation of the repertoire of TA IMPs
295 found in each organism. For both yeast and humans, the majority of proteins have no annotated
296 cellular localization. Several previously suggested TA IMPs are excluded from this new set
297 including, for example, OTOA (otoancorin) that contains a likely signal sequence, FDFT1
298 (squalene synthase or SQS) with two predicted hydrophobic helices by this method, and YDL012c
299 which has a TMD with very low hydrophobicity (full list in Table S1) [59,66].
300 Broadly, hydrophobicity is considered a dominant feature for discriminating TA IMP
301 localization with those that contain more hydrophobic TMDs localizing to the ER [67]. We explore
302 this in Fig. 7*B*, where the hydrophobicity of the entire TMD for each yeast TA IMP was calculated
303 using the TM tendency scale [68] and is plotted along the y-axis. If we only consider proteins
304 known to localize to the ER or mitochondria, this analysis classifies the majority of the proteins
305 correctly at a best threshold of 16.8 (red dashed line, Fig. 7*B*). While all five mitochondrial TA
306 IMPs are correctly classified, a significant number of ER-bound TAs contain a TMD with a
307 hydrophobicity lower than the threshold (Fig. 7*B*). A notable misclassified example is Sss1
308 (Sec61γ in chordates) of the ER residing Sec translocon.
309 We next considered whether the hydrophobic face preference of Sgt2/A might be reflected in

310 the ability to classify TA IMPs. For yeast, we calculated the maximum hydrophobicity of a helical
311 face of six amino acids and plotted this value (x-axis, Fig. 7*B*). ER targeted TA IMPs are best
312 classified by a helical face threshold of 7.7 (Fig. 7*B*, cyan dotted line). While both metrics correctly
313 categorize mitochondria-bound TA IMPs (all in lower left quadrant), the helical-face metric better
314 categorizes low hydrophobicity ER bound TA IMPs, *e.g.* Sbh1 is now correctly classified as ER-
315 localized (Fig 7*A*). More quantitatively (Fig. 7*C*), as a predictor the AUROC value for
316 classification based on the hydrophobicity of a single face (AUROC = 0.99) is higher than that
317 based on hydrophobicity of the entire TMD (AUROC = 0.87), supporting the relevance of a
318 hydrophobic face in TA IMP targeting by Sgt2/A.

319 We then applied this analysis to the 587 putative human TA IMPs. Again, proteins were
320 plotted based on the hydrophobicity of the entire TMD (y-axis) and the most hydrophobic face (x-
321 axis) and colored based on UniProt-annotated cellular localization (Fig. 7*D*). The best thresholds
322 determined by our analysis (overall 19.8 and face 9.3) again show that Sec61γ continues to only
323 be correctly categorized by the hydrophobicity of its helical face. As with yeast proteins, an
324 increase in AUROC value was observed when clients were classified based on the hydrophobicity
325 of single face (AUROC = 0.82) instead of the entire TMDs (AUROC = 0.79). With human TA
326 IMPs, a metric focusing on a sufficiently hydrophobic face does just as well if not better than a
327 metric focusing on the hydrophobicity of the TMD. The moderate improvement in predictive
328 capacity likely reveals the higher complexity of the human system and the milder effect of mutants
329 to *Hs*SGTA-C on binding to TA clients.

330 Interestingly, by considering the hydrophobic face, more information can be gleaned about
331 complex clients that localize to both the mitochondria and ER. Notable examples are members of
332 the Bcl-2 family, which play critical roles in the apoptosis pathway [69,70]. Although many have
333 been reported to localize to several organelles in the cell, some have a preferred localization [69,70].
334 For example, Bcl-xL has been reported to localize predominantly to the mitochondria, though a
335 fraction of its cellular concentration has been observed to be present in the ER. The case is similar
336 for McL1 [71] and Bcl-B [70,72]. Classified by their hydrophobic face, these proteins are predicted
337 to be mitochondria-bound clients (blue, Fig. 7*D*). Unlike Bcl-xL, the majority of cellular Bok,
338 another Bcl-2 family member, is found in the ER or Golgi [73]. The hydrophobic face metric
339 classifies Bok as an ER bound protein whereas a metric based on the hydrophobicity of the entire
340 TMD misclassifies it as a mitochondrial protein (Fig. 7*D*). This suggests our metric can correctly

341 determine the primary localization of members of the Bcl-2 family TA IMPs, important insight for
342 these medically relevant proteins.

343 Another interesting case for the identification and localization of TA IMPs is the apparent
344 lack of the protein squalene synthase (SQS) in our list, previously used as a model TA [66]. Since
345 SQS is predicted to have two TMDs, it is excluded by the criteria above. However, structural
346 studies of SQS have clearly identified the predicted first TMD to instead be a helical component
347 of the folded soluble domain [74]; therefore, the protein only contains a single TMD at the C-
348 terminus which would fit the standard definition of a TA IMP. Once again, if we consider the
349 human protein SQS and where its TMD falls on the localization metrics (Fig. 8*C*, red x), the TM
350 tendency of its entire TMD (12.5) predicts it to be mitochondrial while considering the most
351 hydrophobic face (9.9) accurately captures its ER localization. How this protein fits into our
352 understanding of ER localized TA IMPs is discussed below. Future refinement of our
353 bioinformatics screen to include details such as known or predicted structure may further hone the
354 list of putative TA IMPs (Table S1).

355

356 **Discussion**

357 Sgt2/A, the most upstream component of the GET/TRC pathway, plays a critical role in the
358 correct insertion of TA IMPs into their designated membranes. Its importance as the first selection
359 step of ER versus mitochondrial bound TA clients necessitates a molecular model for TA client
360 binding. Previous work demonstrated a role for the C-domain of Sgt2/A to bind to hydrophobic
361 clients, yet the exact binding domain remained to be determined. Through the combined use of
362 biochemistry, bioinformatics, and computational modeling, we conclusively identify the minimal
363 client-binding domain of Sgt2/A. This allowed us to present a validated structural model of Sgt2/A
364 C-domain as a methionine-rich helical hand for grasping a hydrophobic helix providing a
365 mechanistic explanation for binding a minimum TMD of 11 hydrophobic residues with the most
366 hydrophobic residues organized onto one face of the helix.

367 Based on these results, we can confidently identify that the C-domain of Sgt2/A contains a
368 STI1 domain for client binding. This places the protein into a larger context of both conserved co-
369 chaperones and adaptors of the ubiquitin-proteasome system (AUPS) (Fig. 8*A*). For the co-
370 chaperone family, the STI1 domains predominantly follow HSP-binding TPR domains connected
371 by a flexible linker. As noted above, it was demonstrated that Sti1/Hop domains are critical for

372 client-processing and coordinated hand-off between Hsp70 and Hsp90 homologs [75].
373 Additionally, multiple TPR domains of Sti1/Hop are used to coordinate simultaneous binding of
374 two heat shock proteins. Both Sgt2/A and the co-chaperone Hip share the coordination of two TPR
375 and STI1 domains by forming stable dimers via N-terminal dimerization domains [76]. With
376 evidence for a direct role of the carboxylate-clamp in the TPR domain of Sgt2/A for client-binding
377 now clear [21], one can speculate that the two TPR domains may facilitate TA client entry into
378 other pathways using multiple heat shock proteins. The more distant chloroplast Tic40 contains
379 two putative STI1 domains [77,78] (Fig. 8*A*), with the C-terminal one having a structure clearly
380 similar to that of other co-chaperones (Fig. S2*D*). The rest of the protein has a different domain
381 architecture as it lacks a clear TPR domain [78] and has an N-terminal TMD. Found in the inner
382 chloroplast membrane with the STI1 domain(s) in the stroma, the C-terminal domain can be
383 replaced with the STI1 domain from Hip without loss-of-function [79]. How Tic40 fits
384 mechanistically into this group is less clear.

385 As annotated, STI1 domains broadly share several features including four to five amphipathic
386 helices (Fig. 8*A* and Fig. S2*A,B*). For structurally characterized domains, these organize into helical
387 hands with a hydrophobic groove (Fig. 8*B* and Fig. S2). In the co-chaperones, all of the domains
388 have the same architecture and are characterized by structural flexibility in the absence of client.
389 While there are no structures of client-bound STI1 domains for this group, the H0 helix in the
390 structure of the DP1 domain from Sti1 likely mimics client binding (grey helix in Fig. 8*B* and Fig.
391 S2*A*). This N-terminal amphipathic helix is conserved among co-chaperone STI1 domains (Fig.
392 S2*A,C*) and the additional helix may be a general feature. Structurally, the co-chaperone STI1
393 domains contain five core amphipathic helices. Bioinformatics databases, like SMART, use this
394 definition, which can lead to erroneous annotations of putative STI1 domains. The clearest case
395 for this is the two pairs of abutting STI1 motifs predicted for UBQLN -1, -2, & -4. Careful analysis
396 reveals a N-terminal sixth amphipathic helix. When this is considered, it is clear that the abutting
397 STI1 domains are instead a single domain (Fig. S2*B*). While the roles of the additional helices are
398 not clear, they are well conserved within each family. A possible speculation is that they perhaps
399 acts as a lid for protecting the empty groove and/or set the hydrophobic threshold for client-binding,
400 as predicted for other TMD binders [4]. For the AUPS proteins, the only known structure of a STI1
401 domain comes from the DNA damage response protein Rad23. For this domain, the architecture
402 is different with only four helices that form a different hydrophobic groove for recognition of

403 clients (Fig. 8*B*). In fact, this difference is underscored by the poor alignment between Rad23 with
404 STI1 domains (Fig. S2*B,D*). Nonetheless, several structures of complexes of Rad23-STI1 bound
405 to amphipathic clients show in each that the client-helix binds via a hydrophobic face (Fig. 8*B* and
406 Fig. S2*D*). Perhaps this represents a second class of STI1-like domains that could include proteins
407 such as Ddi1 [80,81].

408 The concept of TMD binding by a helical hand is reminiscent of other proteins involved in
409 membrane protein targeting. Like Sgt2/A, the signal recognition particle (SRP) contains a
410 methionine-rich domain that binds signal sequences and TMDs. While the helical order is inverted,
411 again five amphipathic helices form a hydrophobic groove that cradles the client signal [82]. Here
412 once more, the domain has been observed to be flexible in the absence of client [83,84] and, in the
413 resting state, occupied by a region that includes a helix that must be displaced [82]. Another
414 helical-hand example recently shown to be involved in TA-protein targeting is calmodulin where
415 two helical hands coordinate to clasp a TMD from either side (Fig. 9B). Considering an average
416 TMD of 18-20 amino acids (to span a ~40Å bilayer), each half of calmodulin interacts with about
417 10 amino acids. The close correspondence of this value with the minimal binding length for Sgt2/A
418 C-domain leads one to speculate that the two copies of the Sgt2/A C-domain in the dimer may
419 work together to bind to a full TMD. Cooperation of the two Sgt2/A C-domains in client-binding
420 could elicit conformational changes in the complex that would be recognized by downstream
421 factors, such as increasing the affinity for Get5/Ubl4A. Paired STI1 domains in UBQLN-1, -2, &
422 -4 may cooperate as well. Recently, others noted the ability of the SGTA C-domain to
423 independently dimerize in certain conditions, also hinting at a model of cooperation between
424 across the dimers for client binding [47]. While we see no evidence for dimerization of the C-
425 domain in our constructs, it is clear that interactions between C-domains are likely important.

426 What is the benefit of the flexible helical-hand structure for hydrophobic helix binding? While
427 it remains an open question, it is notable that evolution has settled on similar simple solutions to
428 the complex problem of specific but temporary binding of hydrophobic helices. For all of the
429 domains mentioned, the flexible helical-hands provide an extensive hydrophobic surface to capture
430 the client-helix—driven by the hydrophobic effect. Typically, such extensive interfaces are
431 between pairs of pre-ordered surfaces resulting in very stable binding. Required to only engage
432 temporarily, the flexibility of the helical hand offsets the favorable free energy of binding by
433 charging an additional entropic cost from the need to transition from a flexible unbound form to

434 that in the client-bound complex. This would account for the favorable transfer seen from Sgt2 [21]
435 and SGTA [85] to downstream components.

436 While SGTA and Sgt2 share many properties, there are a number of differences between the
437 two proteins that may explain the different biochemical behavior. For the C_{cons}-domains, SGTA
438 appears to be more ordered in the absence of client as the peaks in its NMR spectra are broader
439 (Fig. 1*E*). Comparing the domains at the sequence level, while the high glutamine content in the
440 C-domain is conserved it is higher in SGTA (8.8% versus 15.2%). The additional glutamines are
441 concentrated in the predicted longer H4 helix (Fig. 1*A*). The linker to the TPR domain is shorter
442 compared to Sgt2 while the loop between H3 and H4 is longer. Do these differences reflect
443 different roles? As noted, in every case the threshold for hydrophobicity of client-binding is lower
444 for SGTA than Sgt2 (Fig. 1*E*, 5, and 6) implying that SGTA is more permissive in client binding.
445 The two C-domains have similar hydrophobicity, so this difference in binding might be due to a
446 lower entropic cost paid by having the SGTA C-domain more ordered in the absence of client.

447 An interesting exception is SQS, which is a client of the EMC, rather than the TRC pathway
448 [66]. The EMC pathway is characterized as targeting ER TA clients of lower hydrophobicity due
449 to a higher affinity of its chaperone calmodulin for these clients over SGTA. Based on experimental
450 results, a threshold for EMC dependence lies approximately at 21.6 [66], slightly higher than the
451 overall hydrophobicity cut-off noted here for ER prediction (Fig. 7*C*). By this metric,
452 mitochondrial and EMC dependent TA clients are indistinguishable. Putative EMC client
453 localization is more accurately predicted by the hydrophobic face metric (ER proteins in the lower
454 right quadrant of Fig. 7*D*). The increased hydrophobicity of TRC/GET pathway clients results in
455 more hydrophobic residues in their TMDs leading to consistently higher values in the hydrophobic
456 face metric. Yet, our analysis reveals the importance of a hydrophobic face for discriminating ER
457 versus mitochondria targeted TAs with low hydrophobicity. As current evidence favors a
458 dependence on the EMC pathway for the ER proteins, one might speculate either a continued role
459 for SGTA for these clients or that the helical-hands of calmodulin also favor hydrophobic face
460 binding. The latter seems unlikely as a discriminatory step as calmodulin is a generalist in client
461 binding [86]. In the absence of calmodulin, SGTA is sufficient for delivering TA clients to the
462 EMC [66] and perhaps acts upstream of calmodulin to discriminate between ER and mitochondrial
463 targets.

464 The targeting of TA clients presents an intriguing and enigmatic problem for understanding

465 the biogenesis of IMPs. How subtle differences in each client modulates the interplay of hand-offs
466 that direct these proteins to the correct membrane remains to be understood. In this study, we focus
467 on a central player, Sgt2/A and its client-binding domain. Through biochemistry and computational
468 analysis, we provide more clarity to client discrimination. A major outcome of this is the clear
469 preference for a hydrophobic face on ER TA IMPs of low hydrophobicity. In yeast, this alone is
470 sufficient to predict the destination of a TA IMP. In mammals, and likely more broadly in
471 metazoans, while clearly an important component, alone the hydrophobic face cannot fully
472 discriminate targets. For a full understanding, we expect other factors to contribute reflective of
473 the increased complexity of higher eukaryotes, perhaps involving more players [87]. Suffice to say,
474 this study highlights the important role of Sgt2/A in TA IMP biogenesis.

475 # Material and Methods

476 **Plasmid constructs**

477 MBP-Sbh1, *Sc*Sgt2$_{95\text{-}346}$ (*Sc*Sgt2-TPR-C), *Sc*Sgt2$_{222\text{-}346}$ (*Sc*Sgt2-C), *Sc*Sgt2$_{260\text{-}327}$ (*Sc*Sgt2-
478 C$_{cons}$), *Sc*Sgt2$_{266\text{-}327}$ (*Sc*Sgt2-ΔH0), *Hs*SGTA$_{87\text{-}313}$ (*Hs*SGTA-TPR-C), *Hs*SGTA$_{213\text{-}313}$ (*Hs*SGTA-C),
479 *Hs*SGTA$_{219\text{-}300}$ (*Hs*SGTA-C$_{cons}$), and *Hs*SGTA$_{228\text{-}300}$ (*Hs*SGTA-ΔH0) were prepared as previously
480 described [12,88]. Genes of *ScSgt2* or *Hs*SGTA variants were amplified from constructed plasmids
481 and then ligated into an pET33b-derived vector with a 17 residue N-terminal hexa-histidine tag
482 and a tobacco etch virus (TEV) protease site. Single or multiple mutations on Sgt2/A were
483 constructed by site-direct mutagenesis. Artificial TAs were constructed in a pACYC-Duet plasmid
484 with a N-terminal cMyc tag, BRIL protein [89], GSS linker, and a hydrophobic C-terminal tail.

485 **Protein expression and purification**

486 All proteins were expressed in *Escherichia coli* NiCo21 (DE3) (New England BioLabs). To
487 co-express multiple proteins, constructed plasmids were co-transformed as described [88]. Protein
488 expression was induced by 0.3 mM IPTG at OD_{600} ~ 0.7 and harvested after 3 hours at 37°C. For
489 structural analysis, cells were lysed through an M-110L Microfludizer Processor (Microfluidics)
490 in lysis buffer (50 mM Tris, 300 mM NaCl, 25 mM imidazole supplemented with benzamidine,
491 PMSF, and 10 mM β-ME, pH 7.5). For capture assays, cells were lysed by freeze-thawing 3 times
492 with 0.1 mg/mL lysozyme. To generate endogenous proteolytic products of *Sc*Sgt2-TPR-C for MS
493 analysis, PMSF and benzamidine were excluded from the lysis buffer. His-Sgt2/A and their
494 complexes were separated from the lysate by batch incubation with Ni-NTA resin at 4°C for 1hr.
495 The resin was washed with 20 mM Tris, 150 mM NaCl, 25 mM imidazole, 10 mM β-ME, pH 7.5.
496 The complexes of interest were eluted in 20 mM Tris, 150 mM NaCl, 300 mM imidazole, 10 mM
497 β-ME, pH 7.5.

498 For structural analysis, the affinity tag was removed from complexes collected after the nickel
499 elution by an overnight TEV digestion against lysis buffer followed by size-exclusion
500 chromatography using a HiLoad 16/60 Superdex 75 prep grade column (GE Healthcare).

501 Measurement of Sgt2/A protein concentration was carried out using the bicinchoninic acid
502 (BCA) assay with bovine serum albumin as standard (Pierce Chemical Co.). Samples for NMR
503 and CD analyses were concentrated to 10-15 mg/mL for storage at −80°C before experiments.

504 **NMR Spectroscopy**

505 ^{15}N-labeled proteins were generated from cells grown in auto-induction minimal media as
506 described [90] and purified in 20 mM phosphate buffer, pH 6.0 (for ScSgt2-C, 10mM Tris, 100mM
507 NaCl, pH 7.5). The NMR measurements of ^{15}N-labeled Sgt2/A-C proteins (~0.3-0.5 mM) were
508 collected using a Varian INOVA 600 MHz spectrometer at either 25°C (*Sc*Sgt2-C) or 35°C
509 (*Hs*SGTA-C) with a triple resonance probe and processed with TopSpin™ 3.2 (Bruker Co.).

510 **CD Spectroscopy**

511 The CD spectrum was recorded at 24°C with an Aviv 202 spectropolarimeter using a 1 mm
512 path length cuvette with 10 μM protein in 20 mM phosphate buffer, pH 7.0. The CD spectrum of
513 each sample was recorded as the average over three scans from 190 to 250 nm in 1 nm steps. Each
514 spectrum was then decomposed into its most probable secondary structure elements using BeStSel
515 [91].

516 **Glu-C digestion of the double Cys mutants on *Sc*Sgt2-C**

517 Complexes of the co-expressed wild type or double Cys mutated His-*Sc*Sgt2-TPR-C and the
518 artificial TA, 11[L8], were purified as the other His-Sgt2/A complexes described above. The
519 protein solutions were mixed with 0.2 mM $CuSO_4$ and 0.4 mM 1,10-phenanthroline at 24°C for
520 20 min followed by 50 mM N-ethyl maleimide for 15 min. Sequencing-grade Glu-C protease
521 (Sigma) was mixed with the protein samples at an approximate ratio of 1:30 and the digestion was
522 conducted at 37°C for 22 hours. Digested samples were mixed with either non-reducing or
523 reducing SDS-sample buffer, resolved via SDS-PAGE using Mini-Protean® Tris-Tricine Precast
524 Gels (10-20%, Bio-Rad), and visualized using Coomassie Blue staining.

525 **Protein immunoblotting and detection**

526 For western blots, protein samples were resolved via SDS-PAGE and then transferred onto
527 nitrocellulose membranes by the Trans-Blot® Turbo™ Transfer System (Bio-Rad). Membranes
528 were blocked in 5% non-fat dry milk and hybridized with antibodies in TBST buffer (50 mM Tris-
529 HCl pH 7.4, 150 mM NaCl, 0.1% Tween 20) for 1 hour of each step at 24°C. The primary
530 antibodies were used at the following dilutions: 1:1000 anti-penta-His mouse monoclonal (Qiagen)
531 and 1:5000 anti-cMyc mouse monoclonal (Sigma). A secondary antibody conjugated to alkaline
532 phosphatase (Rockland, 1:8000) was employed, and the blotting signals were chemically
533 visualized with NBT/BCIP (Sigma). All blots were photographed and quantified by image

534 densitometry using ImageJ [92] or ImageStudioLite (LI-COR Biosciences).

535 **Quantification of Sgt2/A—TA complex formation**

536 The densitometric analysis of MBP-Sbh1 capture by His-Sgt2/A quantified the intensity of
537 the corresponding protein bands on a Coomassie Blue G-250 stained gel. The quantified signal
538 ratios of MBP-Sbh1/His-Sgt2 are normalized to the ratio obtained from the wild-type (WT).
539 Expression level of MBP-Sbh1 was confirmed by immunoblotting the MBP signal in cell lysate.
540 Average ratios and standard deviations were obtained from 3-4 independent experiments.

541 In artificial TA experiments, both his-tagged Sgt2/A and cMyc-tagged artificial TAs were
542 quantified via immunoblotting signals. The complex efficiency of Sgt2/A with various TAs was
543 obtained by

544 $$E_{complex} = \frac{E_{TA}}{T_{TA}} \times \frac{1}{E_{capture}} \quad (1)$$

545 where E_{TA} is the signal intensity of an eluted TA representing the amount of TA co-purified with
546 Sgt2/A. T_{TA} is the signal intensity of a TA in total lysate that corresponds to the expression yield
547 of that TA. Identical volumes of elution and total lysate from different TAs experiments were
548 analyzed and quantified. In order to correct for possible variation in Ni-NTA capture efficiencies,
549 $E_{capture}$ is applied and were obtained by

550

551 $$E_{capture} = \frac{E_{Sgt2}}{E_{purified,\ Sgt2}}, \quad (2)$$

552

553 where E_{Sgt2} is the signal intensity of eluted Sgt2/A, and $E_{purified,\ Sgt2}$ is purified His-tagged Sgt2-
554 TPR-C as an external control. Each E_{TA} and T_{TA} was obtained by blotting both simultaneously, *i.e.*
555 adjacently on the same blotting paper. To facilitate comparison between TAs, the TA complex
556 efficiency $E_{complex,\ TA}$ is normalized by Bos1 complex efficiency $E_{complex,\ Bos1}$.

557 $$\%\ Complex = \frac{E_{complex,\ TA}}{E_{complex,\ Bos1}} \times 100 \quad (3)$$

558 **Molecular modeling**

559 Putative models for *Sc*Sgt2-C were generated with I-TASSER, PCONS, Quark, and Rosetta
560 via their respective web servers [48-51]. Residue proximity probed by disulfide bond formation
561 suggests that the models put forth by Quark are most plausible. These structures were the only
562 ones with a potential binding groove. The highest scoring model was then chosen to identify

563 putative TA binding sites. To generate complexes, various transmembrane domains were modelled
564 as alpha helices (using 3D-HM [93]) and rigid-body docked into the Sgt2-C_{cons} through the Zdock
565 web server [94]. Images were rendered using PyMOL 2.2 (www.pymol.org).
566 Using the same set of structure prediction servers, we were unable to produce a clear structural
567 model for SGTA-C. We were also unable to get a convincing model by threading the SGTA-C
568 sequence onto the Sgt2-C model [95].

569 **Structure Relaxation**

570 The highest scoring model of Sgt2-C from Quark was relaxed by all-atom molecular
571 dynamics to better account for molecular details not explicitly accounted for by structure
572 prediction methods, *i.e.* to understand an energetic local minimum near the prediction. The protein
573 and solvent system (TIP3P, ~12k atoms, CHARMM36 [96]) once built was minimized (500 steps)
574 and slowly heated to 298K (0.01K/fs) twice: first with a 10 kJ/mol/$Å^2$ harmonic restraint on each
575 protein atom and then without restraints. The resulting system was equilibrated for 2 ns at constant
576 volume and then for 100 ns at constant pressure (1 atm). All manipulation and calculations were
577 performed using VMD 1.9.2 [97] and NAMD 2.11 [98]. Further details about the simulation
578 protocols and results can be found within the configuration or output files (details below).

579 **Assembling a database of putative tail-anchored proteins and their TMDs**

580 Proteins identified from UniProt [60] containing a single transmembrane domain within 30
581 residues of the C-terminus were separated into groups based on their localization reported in
582 UniProt. The topology of all proteins with 3 TMs or fewer was further analyzed using TOPCONS
583 [61] to avoid missed single-pass TM proteins. Proteins with a predicted signal peptide [63], an
584 annotated transit peptide, problematic cautions, or with a length less than 50 or greater than 1000
585 residues were excluded. Proteins localized to the ER, golgi apparatus, nucleus, endosome,
586 lysosome, and cell membrane were classified as ER-bound, those localized to the outer
587 mitochondrial membrane were classified as mitochondria-bound, those localized to the
588 peroxisome were classified as peroxisomal proteins, and those with unknown localization were
589 classified as unknown. Proteins with a compositional bias overlapping with the predicted TMD
590 were also excluded. A handful of proteins and their inferred localizations were manually corrected
591 or removed (see notebook and Table S1).
592

593 **Assessing the predictive power of various hydrophobicity metrics**

594 We thoroughly examined the metrics relating hydrophobicity, both published and by our own
595 exploration, to better understand their relationship to protein localization. Notably, we recognized
596 that a TMD's hydrophobic moment $\langle \mu_H \rangle$ [99] was a poor predictor of localization, *e.g.* although
597 a Leu_{18} helix is extremely hydrophobic, it has $\langle \mu_H \rangle = 0$ since opposing hydrophobic residues are
598 penalized in this metric. To address this, we define a metric that capture the presence of a
599 hydrophobic face of the TMD: the maximally hydrophobic cluster on the face. For this metric we
600 sum the hydrophobicity of residues that orient sequentially on one side of a helix when visualized
601 in helical wheel diagram. While a range of hydrophobicity scales were predictive using this metric,
602 we selected the TM Tendency scale [68] to characterize the TMDs of putative TA IMPs and
603 determined the most predictive window by assessing a range of lengths from 4 to 12 (this would
604 vary from three turns of a helix to six).

605 By considering sequences with inferred ER or mitochondrial localizations, we calculated the
606 Area Under the Curve of a Receiver Operating Characteristic (AUROC) to assess predictive power.
607 As we are comparing a real-valued metric (hydrophobicity) to a 2-class prediction, the AUROC is
608 better suited for this analysis over others like accuracy or precision (a primer [100]). Due to many
609 fewer mitochondrial proteins (*i.e.* a class imbalance), we also confirmed that the AUROC values
610 were consistent with the more robust, but less common, Average Precision (see notebook).

611 **Sequence analyses**

612 An alignment of Sgt2-C domains was carried out as follows: all sequences with an annotated
613 N-terminal Sgt2/A dimerization domain (PF16546 [101]), at least one TPR hit (PF00515.27,
614 PF13176.5, PF07719.16, PF13176.5, PF13181.5), and at least 50 residues following the TPR
615 domain were considered family members. Putative C-domains were inferred as all residues
616 following the TPR domain, filtered at 90% sequence identity using CD-HIT [102], and then
617 aligned using MAFFT G-INS-i [103]. Other attempts with a smaller set (therefore more divergent)
618 of sequences results in an ambiguity in the relative register of H0, H1, H2, and H3 when comparing
619 Sgt2 with SGTA.

620 Alignments of Sti1 (DP1/DP2) and STI1 domains were created by pulling all unique domain
621 structures with annotated STI1 domains from Uniprot. Where present, the human homolog was
622 selected and then aligned with PROMALS3D [104]. PROMALS3D provides a way of integrating

a variety of costs into the alignment procedure, including 3D structure, secondary structure predictions, and known homologous positions.

All alignments were visualized using Jalview [105]. See code repository for additional details.

Data and Code Availability

All configuration, analysis, and figure generation code employed is available openly at github.com/clemlab/sgt2a-modeling with analysis done in Jupyter Lab/Notebooks using Python 3.6 enabled by Numpy, Pandas, Scikit-Learn, BioPython, and Bokeh [106-111]. The system topology and output files (including trajectory sampled at 0.5 ns intervals) can be permanently found here: 10.22002/D1.1100

Acknowledgements

We thank D. G. VanderVelde for assistance with NMR data collection; S. Mayo for providing computing resources; S.-o. Shan, H. J. Cho, and members of the Clemons lab for support and discussion. We thank J.-Y. Mock and A. M. Thinn for comments on the manuscript. This work was supported by the National Institutes of Health (NIH) Pioneer Award 5DP1GM105385 and Grant R01GM097572 (to WMC), NIH/National Research Service Award Training Grant 5T32GM07616 (to SMS and MYF), and a National Science Foundation Graduate Research fellowship under Grant 1144469 (to SMS).

640 ## References

641 1. Pieper U, Schlessinger A, Kloppmann E, Chang GA, Chou JJ, Dumont ME, Fox BG,
642 Fromme P, Hendrickson WA, Malkowski MG, et al. (2013) Coordinating the impact of
643 structural genomics on the human α-helical transmembrane proteome. *Nat Struct Mol*
644 *Biol* **20**: 135–138.
645 2. Aviram N, Schuldiner M (2017) Targeting and translocation of proteins to the
646 endoplasmic reticulum at a glance. *J Cell Sci* **130**: 4079–4085.
647 3. Shao S, Hegde RS (2011) Membrane Protein Insertion at the Endoplasmic Reticulum.
648 *Annu Rev Cell Dev Biol* **27**: 25–56.
649 4. Guna A, Hegde RS (2018) Transmembrane Domain Recognition during Membrane
650 Protein Biogenesis and Quality Control. *Curr Biol* **28**: R498–R511.
651 5. Kutay U, Hartmann E, Rapoport TA (1993) A class of membrane proteins with a C-
652 terminal anchor. *Trends Cell Biol* **3**: 72–75.
653 6. Hegde RS, Keenan RJ (2011) Tail-anchored membrane protein insertion into the
654 endoplasmic reticulum. *Nat Rev Mol Cell Biol* **12**: 787–798.
655 7. Denic V (2012) A portrait of the GET pathway as a surprisingly complicated young
656 man. *Trends Biochem Sci* **37**: 411–417.
657 8. Wattenberg B, Lithgow T (2001) Targeting of C-Terminal (Tail)-Anchored Proteins:
658 Understanding how Cytoplasmic Activities are Anchored to Intracellular Membranes.
659 *Traffic* **2**: 66–71.
660 9. Chartron JW, Clemons WM, Suloway CJM (2012) The complex process of GETting
661 tail-anchored membrane proteins to the ER. *Curr Opin Struct Biol* **22**: 217–224.
662 10. Chio US, Cho H, Shan S-O (2017) Mechanisms of Tail-Anchored Membrane Protein
663 Targeting and Insertion. *Annu Rev Cell Dev Biol* **33**: 417–438.
664 11. Shao S, Hegde RS (2011) A Calmodulin-Dependent Translocation Pathway for Small
665 Secretory Proteins. *Cell* **147**: 1576–1588.
666 12. Chartron JW, Gonzalez GM, Clemons WM Jr. (2011) A Structural Model of the Sgt2
667 Protein and Its Interactions with Chaperones and the Get4/Get5 Complex. *J Biol Chem*
668 **286**: 34325–34334.
669 13. Wang F, Brown EC, Mak G, Zhuang J, Denic V (2010) A Chaperone Cascade Sorts
670 Proteins for Posttranslational Membrane Insertion into the Endoplasmic Reticulum. *Mol*
671 *Cell* **40**: 159–171.
672 14. Simon AC, Simpson PJ, Goldstone RM, Krysztofinska EM, Murray JW, High S,
673 Isaacson RL (2013) Structure of the Sgt2/Get5 complex provides insights into GET-
674 mediated targeting of tail-anchored membrane proteins. *Proc Natl Acad Sci USA* **110**:
675 1327–1332.
676 15. Xu Y, Cai M, Yang Y, Huang L, Ye Y (2012) SGTA Recognizes a Noncanonical
677 Ubiquitin-like Domain in the Bag6-Ubl4A-Trc35 Complex to Promote Endoplasmic
678 Reticulum-Associated Degradation. *Cell Rep* **2**: 1633–1644.
679 16. Wunderley L, Leznicki P, Payapilly A, High S (2014) SGTA regulates the cytosolic
680 quality control of hydrophobic substrates. *J Cell Sci* **127**: 4728–4739.
681 17. Leznicki P, High S (2012) SGTA antagonizes BAG6-mediated protein triage. *Proc Natl*
682 *Acad Sci USA* **109**: 19214–19219.
683 18. Gristick HB, Rao M, Chartron JW, Rome ME, Shan S-O, Clemons WM (2014) Crystal
684 structure of ATP-bound Get3–Get4–Get5 complex reveals regulation of Get3 by Get4.
685 *Nat Struct Mol Biol* **21**: 437–442.

686 19. Mock J-Y, Chartron JW, Zaslaver M, Xu Y, Ye Y, Clemons WM Jr. (2015) Bag6
687 complex contains a minimal tail-anchor–targeting module and a mock BAG domain.
688 *Proc Natl Acad Sci USA* **112**: 106–111.
689 20. Wang F, Whynot A, Tung M, Denic V (2011) The Mechanism of Tail-Anchored Protein
690 Insertion into the ER Membrane. *Mol Cell* **43**: 738–750.
691 21. Cho H, Shan S-O (2018) Substrate relay in an Hsp70-cochaperone cascade safeguards
692 tail-anchored membrane protein targeting. *EMBO J* **37**:.
693 22. Stefer S, Reitz S, Wang F, Wild K, Pang Y-Y, Schwarz D, Bomke J, Hein C, Löhr F,
694 Bernhard F, et al. (2011) Structural basis for tail-anchored membrane protein biogenesis
695 by the Get3-receptor complex. *Science* **333**: 758–762.
696 23. Rome ME, Chio US, Rao M, Gristick H, Shan S-O (2014) Differential gradients of
697 interaction affinities drive efficient targeting and recycling in the GET pathway. *Proc*
698 *Natl Acad Sci USA* **111**: E4929–E4935.
699 24. Vilardi F, Lorenz H, Dobberstein B (2011) WRB is the receptor for TRC40/Asna1-
700 mediated insertion of tail-anchored proteins into the ER membrane. *J Cell Sci* **124**:
701 1301–1307.
702 25. Yamamoto Y, Sakisaka T (2012) Molecular Machinery for Insertion of Tail-Anchored
703 Membrane Proteins into the Endoplasmic Reticulum Membrane in Mammalian Cells.
704 *Mol Cell* **48**: 387–397.
705 26. Schuldiner M, Metz J, Schmid V, Denic V, Rakwalska M, Schmitt HD, Schwappach B,
706 Weissman JS (2008) The GET Complex Mediates Insertion of Tail-Anchored Proteins
707 into the ER Membrane. *Cell* **134**: 634–645.
708 27. Kiktev DA, Patterson JC, Müller S, Bariar B, Pan T, Chernoff YO (2012) Regulation of
709 chaperone effects on a yeast prion by cochaperone Sgt2. *Mol Cell Biol* **32**: 4960–4970.
710 28. Xu Y, Liu Y, Lee J-G, Ye Y (2013) A Ubiquitin-like Domain Recruits an Oligomeric
711 Chaperone to a Retrotranslocation Complex in Endoplasmic Reticulum-associated
712 Degradation. *J Biol Chem* **288**: 18068–18076.
713 29. Rodrigo-Brenni MC, Gutierrez E, Hegde RS (2014) Cytosolic Quality Control of
714 Mislocalized Proteins Requires RNF126 Recruitment to Bag6. *Mol Cell* **55**: 227–237.
715 30. Hessa T, Sharma A, Mariappan M, Eshleman HD, Gutierrez E, Hegde RS (2011) Protein
716 targeting and degradation are coupled for elimination of mislocalized proteins. *Nature*
717 **475**: 394–397.
718 31. Dupzyk A, Williams JM, Bagchi P, Inoue T, Tsai B (2017) SGTA-Dependent
719 Regulation of Hsc70 Promotes Cytosol Entry of Simian Virus 40 from the Endoplasmic
720 Reticulum. *J Virol* **91**: 23.
721 32. Long P, Samnakay P, Jenner P, Rose S (2012) A yeast two-hybrid screen reveals that
722 osteopontin associates with MAP1A and MAP1B in addition to other proteins linked to
723 microtubule stability, apoptosis and protein degradation in the human brain. *Eur J*
724 *Neurosci* **36**: 2733–2742.
725 33. Trotta AP, Need EF, Selth LA, Chopra S, Pinnock CB, Leach DA, Coetzee GA, Butler
726 LM, Tilley WD, Buchanan G (2013) Knockdown of the cochaperone SGTA results in
727 the suppression of androgen and PI3K/Akt signaling and inhibition of prostate cancer
728 cell proliferation. *Int J Cancer* **133**:.
729 34. Buchanan G, Ricciardelli C, Harris JM, Prescott J, Yu ZCL, Jia L, Butler LM, Marshall
730 VR, Scher HI, Gerald WL, et al. (2007) Control of Androgen Receptor Signaling in

731 Prostate Cancer by the Cochaperone Small Glutamine Rich Tetratricopeptide Repeat
732 Containing Protein. *Cancer Res* **67**: 10087–10096.
733 35. Wang H, Zhang Q, Zhu D (2003) hSGT interacts with the N-terminal region of
734 myostatin. *Biochem Biophys Res Commun* **311**: 877–883.
735 36. Chartron JW, VanderVelde DG, Clemons WM Jr. (2012) Structures of the Sgt2/SGTA
736 Dimerization Domain with the Get5/UBL4A UBL Domain Reveal an Interaction that
737 Forms a Conserved Dynamic Interface. *Cell Rep* **2**: 1620–1632.
738 37. Liou S-T, Wang C (2005) Small glutamine-rich tetratricopeptide repeat-containing
739 protein is composed of three structural units with distinct functions. *Arch Biochem*
740 *Biophys* **435**: 253–263.
741 38. Cziepluch C, Kordes E, Poirey R, Grewenig A, Rommelaere J, Jauniaux JC (1998)
742 Identification of a novel cellular TPR-containing protein, SGT, that interacts with the
743 nonstructural protein NS1 of parvovirus H-1. *J Virol* **72**: 4149–4156.
744 39. Callahan MA, Handley MA, Lee YH, Talbot KJ, Harper JW, Panganiban AT (1998)
745 Functional interaction of human immunodeficiency virus type 1 Vpu and Gag with a
746 novel member of the tetratricopeptide repeat protein family. *J Virol* **72**: 5189–5197.
747 40. Winnefeld M, Grewenig A, Schn lzer M, Spring H, Knoch TA, Gan EC, Rommelaere J,
748 Cziepluch C (2006) Human SGT interacts with Bag-6/Bat-3/Scythe and cells with
749 reduced levels of either protein display persistence of few misaligned chromosomes and
750 mitotic arrest. *Exp Cell Res* **312**: 2500–2514.
751 41. Darby JF, Krysztofinska EM, Simpson PJ, Simon AC, Leznicki P, Sriskandarajah N,
752 Bishop DS, Hale LR, Alfano C, Conte MR, et al. (2014) Solution Structure of the SGTA
753 Dimerisation Domain and Investigation of Its Interactions with the Ubiquitin-Like
754 Domains of BAG6 and UBL4A. *PLoS ONE* **9**: e113281–19.
755 42. Dutta S, Tan Y-J (2008) Structural and functional characterization of human SGT and its
756 interaction with Vpu of the human immunodeficiency virus type 1. *Biochemistry* **47**:
757 10123–10131.
758 43. Leznicki P, Korac-Prlic J, Kliza K, Husnjak K, Nyathi Y, Dikic I, High S (2015)
759 Binding of SGTA to Rpn13 selectively modulates protein quality control. *J Cell Sci* **128**:
760 3187–3196.
761 44. Waheed AA, MacDonald S, Khan M, Mounts M, Swiderski M, Xu Y, Ye Y, Freed EO
762 (2016) The Vpu-interacting Protein SGTA Regulates Expression of a Non- glycosylated
763 Tetherin Species. *Sci Rep* **6**: 1–14.
764 45. Luo P, Baldwin RL (1997) Mechanism of helix induction by trifluoroethanol: a
765 framework for extrapolating the helix-forming properties of peptides from
766 trifluoroethanol/water mixtures back to water. *Biochemistry* **36**: 8413–8421.
767 46. Dyson HJ, Wright PE (2004) Unfolded Proteins and Protein Folding Studied by NMR.
768 *Chem Rev* **104**: 3607–3622.
769 47. Martínez-Lumbreras S, Krysztofinska EM, Thapaliya A, Spilotros A, Matak-Vinkovic
770 D, Salvadori E, Roboti P, Nyathi Y, Muench JH, Roessler MM, et al. (2018) Structural
771 complexity of the co-chaperone SGTA: a conserved C-terminal region is implicated in
772 dimerization and substrate quality control. *BMC Biol* **16**: 76.
773 48. Xu D, Zhang Y (2012) Ab initio protein structure assembly using continuous structure
774 fragments and optimized knowledge-based force field. *Proteins* **80**: 1715–1735.
775 49. Yang J, Yan R, Roy A, Xu D, Poisson J, Zhang Y (2015) The I-TASSER Suite: protein
776 structure and function prediction. *Nat Methods* **12**: 7–8.

50. Wallner B (2006) Identification of correct regions in protein models using structural, alignment, and consensus information. *Prot Sci* **15**: 900–913.
51. Bradley P, Misura KM, Baker D (2005) Towards high-resolution de novo structure prediction for small proteins. *Science* **309**: 1868–1871.
52. Chun E, Thompson AA, Liu W, Roth CB, Griffith MT, Katritch V, Kunken J, Xu F, Cherezov V, Hanson MA, et al. (2012) Fusion Partner Toolchest for the Stabilization and Crystallization of G Protein-Coupled Receptors. *Cell Struct Funct* **20**: 967–976.
53. Mallick P, Boutz DR, Eisenberg D, Yeates TO (2002) Genomic evidence that the intracellular proteins of archaeal microbes contain disulfide bonds. *Proc Natl Acad Sci USA* **99**: 9679–9684.
54. Letunic I, Doerks T, Bork P (2015) SMART: recent updates, new developments and status in 2015. *Nucleic Acids Res* **43**: D257–D260.
55. Schmid AB, Lagleder S, Gräwert MA, Röhl A, Hagn F, Wandinger SK, Cox MB, Demmer O, Richter K, Groll M, et al. (2012) The architecture of functional modules in the Hsp90 co-chaperone Sti1/Hop. *EMBO J* **31**: 1506–1517.
56. Li Z, Hartl FU, Bracher A (2013) Structure and function of Hip, an attenuator of the Hsp70 chaperone cycle. *Nat Struct Mol Biol* **20**: 929–935.
57. Nelson GM, Huffman H, Smith DF (2003) Comparison of the carboxy-terminal DP-repeat region in teh co-chaperones Hop and Hip. *EMBO J* **8**: 125–133.
58. Rao M, Okreglak V, Chio US, Cho H, Walter P, Shan S-O (2016) Multiple selection filters ensure accurate tail-anchored membrane protein targeting. *eLife* **5**: e21301–e21324.
59. Beilharz T, Egan B, Silver PA, Hofmann K, Lithgow T (2003) Bipartite Signals Mediate Subcellular Targeting of Tail-anchored Membrane Proteins in Saccharomyces cerevisiae. *J Biol Chem* **278**: 8219–8223.
60. Bateman A, Martin MJ, O'Donovan C, Magrane M, Alpi E, Antunes R, Bely B, Bingley M, Bonilla C, Britto R, et al. (2017) UniProt: the universal protein knowledgebase. *Nucleic Acids Res* **45**: D158–D169.
61. Tsirigos KD, Peters C, Shu N, Käll L, Elofsson A (2015) The TOPCONS web server for consensus prediction of membrane protein topology and signal peptides. *Nucleic Acids Res* **43**: W401–W407.
62. Borgese N, Colombo S, Pedrazzini E (2003) The tale of tail-anchored proteins. *J Cell Biol* **161**: 1013–1019.
63. Nielsen H (2017) *Predicting Secretory Proteins with SignalP.* Methods in molecular biology (Clifton, N.J.).
64. Burri L, Lithgow T (2003) A Complete Set of SNAREs in Yeast. *Traffic* **5**: 45–52.
65. Kalbfleisch T, Cambon A, Wattenberg BW (2007) A Bioinformatics Approach to Identifying Tail-Anchored Proteins in the Human Genome. *Traffic* **8**: 1687–1694.
66. Guna A, Volkmar N, Christianson JC, Hegde RS (2018) The ER membrane protein complex is a transmembrane domain insertase. *Science* **359**: 470–473.
67. Guna A, Hegde RS (2018) Transmembrane Domain Recognition during Membrane Protein Biogenesis and Quality Control. *Curr Biol* **28**: R498–R511.
68. Zhao G, London E (2006) An amino acid 'transmembrane tendency' scale that approaches the theoretical limit to accuracy for prediction of transmembrane helices: Relationship to biological hydrophobicity. *Prot Sci* **15**: 1987–2001.

822 69. Schinzel A, Kaufmann T, Borner C (2004) Bcl-2 family members: intracellular
823 targeting, membrane-insertion, and changes in subcellular localization. *Biochim Biophys*
824 *Acta* **1644**: 95–105.
825 70. Popgeorgiev N, Jabbour L, Gillet G (2018) Subcellular Localization and Dynamics of
826 the Bcl-2 Family of Proteins. *Front Cell Dev Biol* **6**: 2468–11.
827 71. Pawlikowska P, Leray I, de Laval B, Guihard S, Kumar R, Rosselli F, Porteu F (2010)
828 ATM-dependent expression of IEX-1 controls nuclear accumulation of Mcl-1 and the
829 DNA damage response. *Cell Death Differ* **17**: 1739–1750.
830 72. Kaufmann T, Schlipf S, Sanz J, Neubert K, Stein R, Borner C (2003) Characterization of
831 the signal that directs Bcl-x L, but not Bcl-2, to the mitochondrial outer membrane. *J*
832 *Cell Biol* **160**: 53–64.
833 73. Echeverry N, Bachmann D, Ke F, Strasser A, Simon HU, Kaufmann T (2013)
834 Intracellular localization of the BCL-2 family member BOK and functional implications.
835 *Cell Death Differ* **20**: 785–799.
836 74. Pandit J, Danley DE, Schulte GK, Mazzalupo S, Pauly TA, Hayward CM, Hamanaka
837 ES, Thompson JF, Harwood HJ Jr. (2000) Crystal Structure of Human Squalene
838 Synthase. *J Biol Chem* **275**: 30610–30617.
839 75. Röhl A, Wengler D, Madl T, Lagleder S, Tippel F, Herrmann M, Hendrix J, Richter K,
840 Hack G, Schmid AB, et al. (2015) Hsp90 regulates the dynamics of its cochaperone Sti1
841 and the transfer of Hsp70 between modules. *Nat Commun* **6**: 6655.
842 76. Coto ALS, Seraphim TV, Batista FAH, Dores-Silva PR, Barranco ABF, Teixeira FR,
843 Gava LM, Borges JC (2018) Structural and functional studies of the Leishmania
844 braziliensis SGT co-chaperone indicate that it shares structural features with HIP and
845 can interact with both Hsp90 and Hsp70 with similar affinities. *Int J Biol Macromol* **118**:
846 693–706.
847 77. Chou M-L, Fitzpatrick LM, Tu S-L, Budziszewski G, Potter-Lewis S, Akita M, Levin
848 JZ, Keegstra K, Li H-M (2003) Tic40, a membrane-anchored co-chaperone homolog in
849 the chloroplast protein translocon. *EMBO J* **22**: 2970–2980.
850 78. Balsera M, Soll J, Buchanan BB (2009) *Chapter 10 - Protein Import in Chloroplasts: An*
851 *Emerging Regulatory Role for Redox*. Elsevier Ltd.
852 79. Bédard J, Trösch R, Wu F, Ling Q, Flores-Pérez Ú, Töpel M, Nawaz F, Jarvis P (2017)
853 Suppressors of the Chloroplast Protein Import Mutant tic40Reveal a Genetic Link
854 between Protein Import and Thylakoid Biogenesis. *Plant Cell* **29**: 1726–1747.
855 80. Trempe J-F, Šašková KG, Sivá M, Ratcliffe CDH, Veverka V, Hoegl A, Ménade M,
856 Feng X, Shenker S, Svoboda M, et al. (2016) Structural studies of the yeast DNA
857 damage-inducible protein Ddi1 reveal domain architecture of this eukaryotic protein
858 family. *Sci Rep* **6**: 33671.
859 81. Sivá M, Svoboda M, Veverka V, Trempe J-F, Hofmann K, Kožíšek M, Hexnerová R,
860 Sedlák F, Belza J, Brynda J, et al. (2016) Human DNA-Damage-Inducible 2 Protein Is
861 Structurally and Functionally Distinct from Its Yeast Ortholog. *Sci Rep* **6**: 30443.
862 82. Voorhees RM, Hegde RS (2015) Structures of the scanning and engaged states of the
863 mammalian SRP-ribosome complex. *eLife* **4**: 1485–21.
864 83. Keenan RJ, Freymann DM, Walter P, Stroud RM (1998) Crystal Structure of the Signal
865 Sequence Binding Subunit of the Signal Recognition Particle. *Cell* **94**: 181–191.

84. Clemons WM, Gowda K, Black SD, Zwieb C, Ramakrishnan V (1999) Crystal structure of the conserved subdomain of human protein SRP54M at 2.1 A resolution: evidence for the mechanism of signal peptide binding. *J Mol Biol* **292**: 697–705.
85. Shao S, Rodrigo-Brenni MC, Kivlen MH, Hegde RS (2017) Mechanistic basis for a molecular triage reaction. *Science* **355**: 298–302.
86. Martoglio B (1997) Signal peptide fragments of preprolactin and HIV-1 p-gp160 interact with calmodulin. *EMBO J* **16**: 6636–6645.
87. Aviram N, Costa EA, Arakel EC, Chuartzman SG, Jan CH, Haßdenteufel S, Dudek J, Jung M, Schorr S, Zimmermann R, et al. (2016) The SND proteins constitute an alternative targeting route to the endoplasmic reticulum. *Nature* **540**: 134–138.
88. Suloway CJ, Rome ME, Clemons WM (2011) Tail-anchor targeting by a Get3 tetramer: the structure of an archaeal homologue. *EMBO J* **31**: 707–719.
89. Chu R, Takei J, Knowlton JR, Andrykovitch M, Pei W, Kajava AV, Steinbach PJ, Ji X, Bai Y (2002) Redesign of a Four-helix Bundle Protein by Phage Display Coupled with Proteolysis and Structural Characterization by NMR and X-ray Crystallography. *J Mol Biol* **323**: 253–262.
90. Studier FW (2005) Protein production by auto-induction in high-density shaking cultures. *Protein Express Purif* **41**: 207–234.
91. Micsonai A, Wien F, Kernya L, Lee Y-H, Goto Y, Réfrégiers M, Kardos J (2015) Accurate secondary structure prediction and fold recognition for circular dichroism spectroscopy. *Proc Natl Acad Sci USA* **112**: E3095–E3103.
92. Schneider CA, Rasband WS, Eliceiri KW (2012) NIH Image to ImageJ: 25 years of image analysis. *Nat Methods* **9**: 671–675.
93. Reißer S, Strandberg E, Steinbrecher T, Ulrich AS (2014) 3D Hydrophobic Moment Vectors as a Tool to Characterize the Surface Polarity of Amphiphilic Peptides. *Biophys J* **106**: 2385–2394.
94. Pierce BG, Wiehe K, Hwang H, Kim BH, Vreven T, Weng Z (2014) ZDOCK server: interactive docking prediction of protein-protein complexes and symmetric multimers. *Bioinformatics* **30**: 1771–1773.
95. Webb B, Sali A (2002) *Comparative Protein Structure Modeling Using MODELLER*. John Wiley & Sons, Inc., Hoboken, NJ, USA.
96. Huang J, MacKerell AD Jr (2013) CHARMM36 all-atom additive protein force field: Validation based on comparison to NMR data. *J Comput Chem* **34**: 2135–2145.
97. Humphrey W, Dalke A, Schulten K (1996) VMD: Visual molecular dynamics. *J Mol Graph* **14**: 33–38.
98. Phillips JC, Braun R, Wang W, Gumbart J, Tajkhorshid E, Villa E, Chipot C, Skeel RD, Kalé L, Schulten K (2005) Scalable molecular dynamics with NAMD. *J Comput Chem* **26**: 1781–1802.
99. Eisenberg D, Weiss RM, Terwilliger TC (1982) The helical hydrophobic moment: a measure of the amphiphilicity of a helix. *Nature* **299**: 371–374.
100. Swets JA, Dawes RM, Monahan J (2000) Better decisions through science. *Sci Am* **283**: 82–87.
101. Finn RD, Coggill P, Eberhardt RY, Eddy SR, Mistry J, Mitchell AL, Potter SC, Punta M, Qureshi M, Sangrador-Vegas A, et al. (2016) The Pfam protein families database: towards a more sustainable future. *Nucleic Acids Res* **44**: D279–D285.

911 102. Li W, Godzik A (2006) Cd-hit: a fast program for clustering and comparing large sets of
912 protein or nucleotide sequences. *Bioinformatics* **22**: 1658–1659.
913 103. Katoh K, Standley DM (2013) MAFFT Multiple Sequence Alignment Software Version
914 7: Improvements in Performance and Usability. *Mol Biol Evol* **30**: 772–780.
915 104. Pei J, Kim B-H, Grishin NV (2008) PROMALS3D: a tool for multiple protein sequence
916 and structure alignments. *Nucleic Acids Res* **36**: 2295–2300.
917 105. Waterhouse AM, Procter JB, Martin DMA, Clamp M, Barton GJ (2009) Jalview Version
918 2--a multiple sequence alignment editor and analysis workbench. *Bioinformatics* **25**:
919 1189–1191.
920 106. Kluyver T, Ragan-Kelley B, Pérez F, Granger B, Bussonnier M, Frederic J, Kelley K,
921 Hamrick J, Grout J, Corlay S, et al. (2016) Jupyter Notebooks -- a publishing format for
922 reproducible computational workflows. In Loizides F, Schmidt B (eds.) pp 87–90.
923 107. Millman KJ, Aivazis M (2011) Python for Scientists and Engineers. *Comput Sci Eng* **13**:
924 9–12.
925 108. McKinney W (2010) Data Structures for Statistical Computing in Python. In pp 51–56.
926 109. Pedregosa F, Varoquaux GEL, Gramfort A, Michel V, Thirion B, Grisel O, Blondel M,
927 Prettenhofer P, Weiss R, Dubourg V, et al. (2011) Scikit-learn: Machine Learning in
928 Python. *J Mach Learn Res* **12**: 2825–2830.
929 110. Cock PJA, Antao T, Chang JT, Chapman BA, Cox CJ, Dalke A, Friedberg I, Hamelryck
930 T, Kauff F, Wilczynski B, et al. (2009) Biopython: freely available Python tools for
931 computational molecular biology and bioinformatics. *Bioinformatics* **25**: 1422–1423.
932 111. Bokeh Development Team (2014) *Bokeh: Python library for interactive visualization*.
933 112. Drozdetskiy A, Cole C, Procter J, Barton GJ (2015) JPred4: a protein secondary
934 structure prediction server. *Nucleic Acids Res* **43**: W389–W394.
935 113. Kyte J, Doolittle RF (1982) A simple method for displaying the hydropathic character of
936 a protein. *J Mol Biol* **157**: 105–132.
937 114. Schägger H (2006) Tricine–SDS-PAGE. *Nat Protoc* **1**: 16–22.
938 115. Fernandez-Patron C, Hardy E, Sosa A, Seoane J, Castellanos L (1995) Double staining
939 of coomassie blue-stained polyacrylamide gels by imidazole-sodium dodecyl sulfate-
940 zinc reverse staining: sensitive detection of coomassie blue-undetected proteins. *Anal*
941 *Biochem* **224**: 263–269.
942 116. Gillespie AS, Elliott E (2005) Comparative advantages of imidazole–sodium dodecyl
943 sulfate–zinc reverse staining in polyacrylamide gels. *Anal Biochem* **345**: 158–160.
944 117. Jones DT (1999) Protein secondary structure prediction based on position-specific
945 scoring matrices. *J Mol Biol* **292**: 195–202.
946 118. Joosten RP, Beek te TAH, Krieger E, Hekkelman ML, Hooft RWW, Schneider R,
947 Sander C, Vriend G (2010) A series of PDB related databases for everyday needs.
948 *Nucleic Acids Res* **39**: D411–D419.
949 119. Thompson JD, Gibson TJ, Plewniak F, Jeanmougin F, Higgins DG (1997) The
950 CLUSTAL_X windows interface: flexible strategies for multiple sequence alignment
951 aided by quality analysis tools. *Nucleic Acids Res* **25**: 4876–4882.
952

953 **Figure Legends**

954 **Fig. 1. Structural characteristics of free Sgt2/A C-domain.** (*A*) *Top*, Schematic of the domain
955 organization of Sgt2/A. *Below,* representative sequences from a large-scale multiple sequence
956 alignment of the C domain: fungal Sgt2 from *S. cerevisiae*, *S. pombe*, and *C. thermophilum* and
957 metazoan SGTA from *C. savignyi*, *X. laevis*, and *H. sapiens*. Protease susceptible sites on *Sc*Sgt2-
958 C identified by mass spectrometry are indicated by red arrowheads. Predicted helices of *Sc*Sgt2
959 (blue) and *Hs*SGTA (orange) by Jpred [112] and/or structure prediction are shown. Blue/orange
960 color scheme for *Sc*Sgt2/*Hs*SGTA is used throughout the text. Residues noted in the text are
961 highlighted by an asterisk. (*B*) Overlay of size-exclusion chromatography traces of *Sc*Sgt2-C (blue
962 line), *Hs*SGTA-C (orange line), *Sc*Sgt2-TPR (blue dash) and *Hs*SGTA-TPR (orange dash). Traces
963 are measured at 214 nm, baseline-corrected and normalized to the same peak height. (*C*) Far UV
964 CD spectrum of 10 μM of purified *Sc*Sgt2-C (blue) and *Hs*SGTA-C (orange) at RT with secondary
965 structure decomposition from BestSel [91]. (*D*) ^{1}H-^{15}N HSQC spectrum of *Sc*Sgt2-C at 25°C. The
966 displayed chemical shift window encompasses all N-H resonances from both backbone and side
967 chains. The range of backbone amide protons, excluding possible side-chain NH_2 of Asn/Gln, is
968 indicated by pairs of red dashed lines. (*E*) As in *D* for *Hs*SGTA-C at 25°C.

969

Figure 1

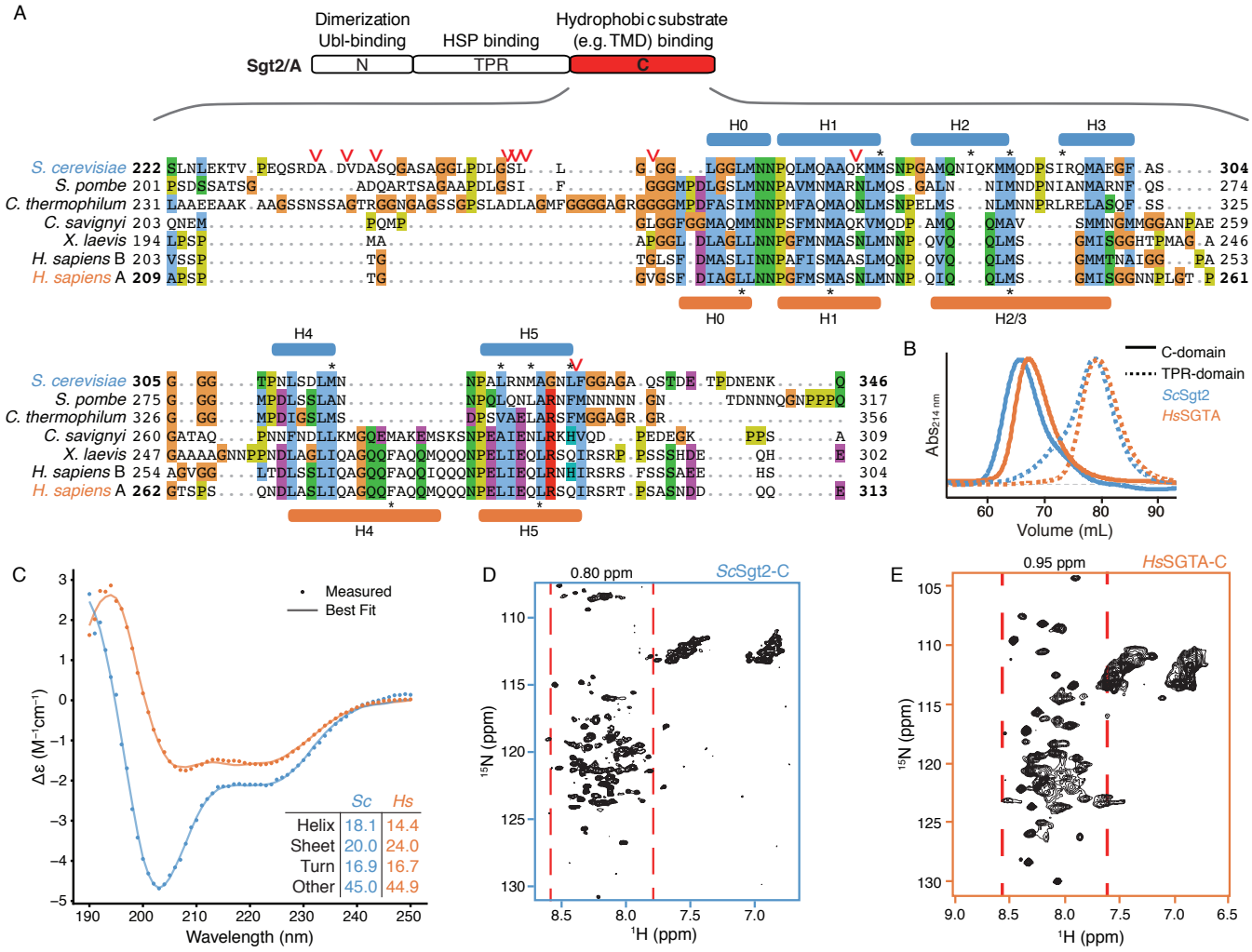
A
Dimerization
Ubl-binding
HSP binding
Hydrophobic substrate
(e.g. TMD) binding
Sgt2/A
N
TPR
C
H0
H1
H2
H3
S. cerevisiae
S. pombe
C. thermophilum
C. savignyi
X. laevis
H. sapiens B
H. sapiens A
H4
H5
H2/3
B
C-domain
TPR-domain
ScSgt2
HsSGTA
Abs214 nm
Volume (mL)
C
Measured
Best Fit
Δε (M⁻¹cm⁻¹)
Wavelength (nm)
Sc
Hs
Helix 18.1 14.4
Sheet 20.0 24.0
Turn 16.9 16.7
Other 45.0 44.9
D
0.80 ppm
ScSgt2-C
15N (ppm)
1H (ppm)
E
0.95 ppm
HsSGTA-C
15N (ppm)
1H (ppm)

971 **Fig. 2. The minimal binding region of Sgt2/A for TA client binding.** (*A*) Diagram of the protein
972 truncations tested for TA binding that include the TPR-C domain, C-domain (C), C_{cons}, and C_{cons}
973 ΔH0 (ΔH0) from *Sc*Sgt2 and *Hs*SGTA. The residues corresponding to each domain are indicated,
974 and grey blocks highlight the C_{cons} region. *(B)* Schematic of capture experiments of MBP-Sbh1 by
975 Sgt2/A TPR-C variants. After co-expression, cell pellets are lysed and NTA-Ni^{2+} is used to capture
976 His-Sgt2/A TPR-C. (*C*) Helical wheel diagrams of predicted helices (see Fig. 1*A*) in the C_{cons}
977 domain of *Sc*Sgt2 and *Hs*SGTA. Residues are colored by the Kyte and Doolittle hydrophobicity
978 scale [113]. (*D*) Tris-Tricine-SDS-PAGE gel [114] of co-expressed and purified MBP-tagged Sbh1
979 and His-tagged Sgt2/A truncations visualized with Coomassie Blue staining. (*E*) Alanine
980 replacement of hydrophobic residues in the C_{cons}. All of the hydrophobic residues (L, I, F, and M)
981 in a predicted helix (H0, H1, etc.) are replaced by Ala and tested for the ability to capture MBP-
982 Sbh1. Protein levels were quantified by Coomassie staining. Relative binding efficiency of MBP-
983 Sbh1 by Sgt2 C-domain variants was calculated relative to total amount of Sgt2 C-domain captured
984 (MBP-Sbh1/Sgt2 C-domain) then normalized to the wild-type Sgt2-C domain. Experiments were
985 performed 3-4 times and the standard deviations are presented. Total expression levels of the MBP-
986 Sbh1 were similar across experiments as visualized by immunoblotting (IB) of the cell lysate. (*F)*
987 As in *E* but for *Hs*SGTA.

988

Figure 2

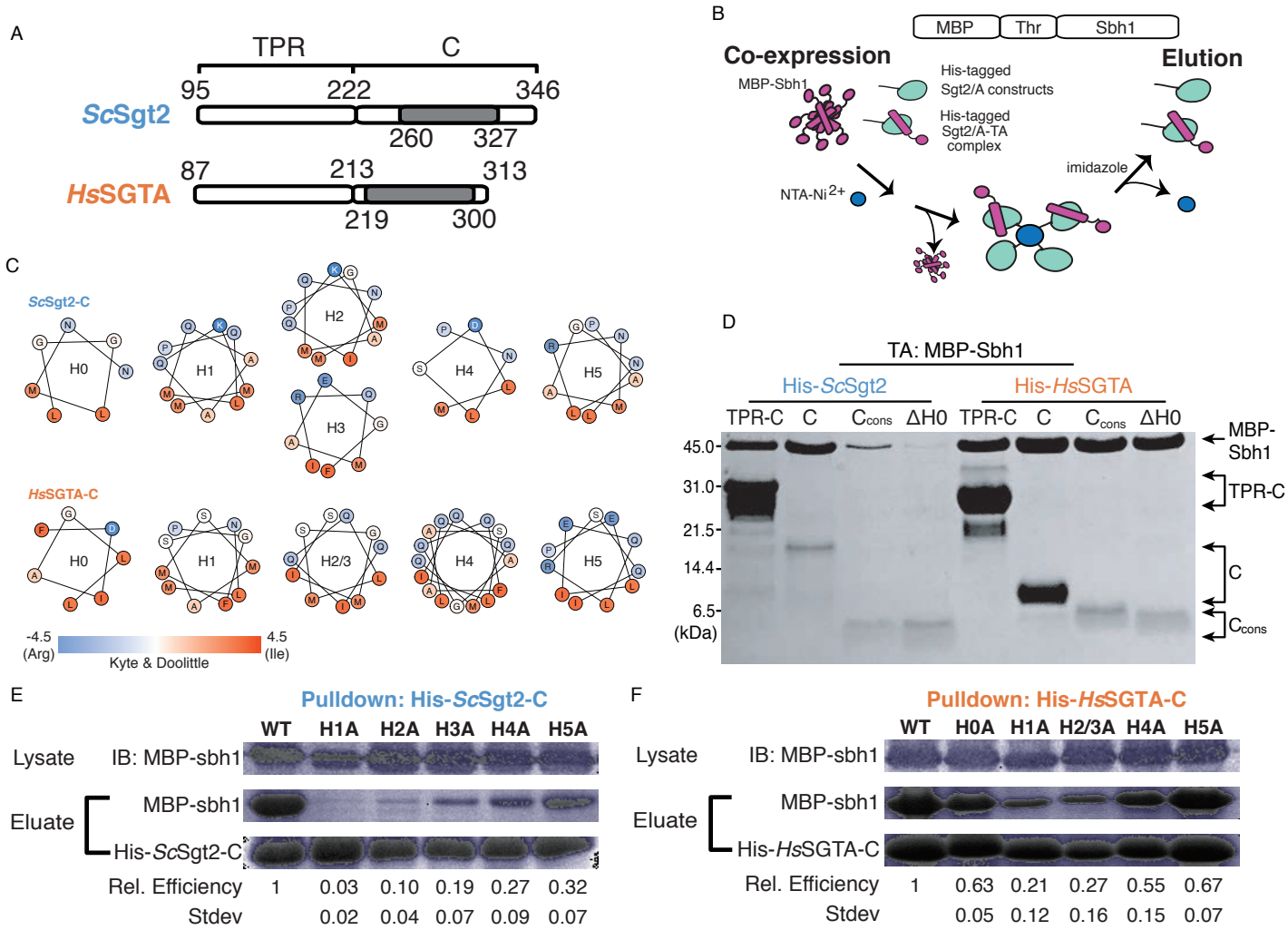
A
TPR
C
95
222
346
ScSgt2
260
327
87
213
313
HsSGTA
219
300
B
MBP
Thr
Sbh1
Co-expression
Elution
MBP-Sbh1
His-tagged Sgt2/A constructs
His-tagged Sgt2/A-TA complex
imidazole
NTA-Ni2+
C
ScSgt2-C
H0
H1
H2
H3
H4
H5
HsSGTA-C
H0
H1
H2/3
H4
H5
-4.5 (Arg)
4.5 (Ile)
Kyte & Doolittle
D
TA: MBP-Sbh1
His-ScSgt2
His-HsSGTA
TPR-C
C
Ccons
ΔH0
TPR-C
C
Ccons
ΔH0
45.0
31.0
21.5
14.4
6.5
(kDa)
MBP-Sbh1
TPR-C
C
Ccons
E
Pulldown: His-ScSgt2-C
WT
H1A
H2A
H3A
H4A
H5A
Lysate
IB: MBP-sbh1
Eluate
MBP-sbh1
His-ScSgt2-C
Rel. Efficiency
1
0.03
0.10
0.19
0.27
0.32
Stdev
0.02
0.04
0.07
0.09
0.07
F
Pulldown: His-HsSGTA-C
WT
H0A
H1A
H2/3A
H4A
H5A
Lysate
IB: MBP-sbh1
Eluate
MBP-sbh1
His-HsSGTA-C
Rel. Efficiency
1
0.63
0.21
0.27
0.55
0.67
Stdev
0.05
0.12
0.16
0.15
0.07

990 **Fig 3. A structural model for Sgt2/A-C_{cons} validated by intramolecular-disulfide bond**
991 **formation.** *(A)* The top 10 models of the Sgt2-C_{cons} generated by the template-free algorithm
992 Quark [48] are overlaid with the highest scoring model in solid. Models are color-ramped from N-
993 (blue) to C-terminus (red). *(B)* A model of Sgt2-C_{cons} (surface colored by Kyte-Doolittle
994 hydrophobicity) bound to a TMD (purple helix) generated by rigid-body docking through Zdock
995 [94]. The darker purple corresponds to an 11 residue stretch. *(C)* The entire Sgt2-C domain from
996 the highest scoring model from Quark (C_{cons} in rainbow with the rest in grey) highlighting H0 and
997 the rest of the flexible termini that vary considerably across models. *(D* and *E)* Variants of His-
998 *Sc*Sgt2-TPR-C (WT or cysteine double mutants) were co-expressed with the artificial TA client,
999 cMyc-BRIL-11[L8]. After lysis, His-*Sc*Sgt2 proteins were purified, oxidized, then digested by
1000 Glu-C protease and analyzed by gel either in non-reducing or reducing buffer. (*E*) Cα ribbon of
1001 *Sc*Sgt2-C_{cons} color-ramped with various pairs of Cysteines highlighted. Scissors indicate protease
1002 cleavage sites resulting in fragments less than 3 kDa in size. (*F*) Tris-Glycine-SDS-PAGE gel
1003 visualized by imidazole-SDS-zinc stain [115,116]. For the WT (cys-free) no significant difference
1004 was found between samples in non-reducing vs. reducing conditions. All close residue pairs
1005 (A272/L327, I286/M323, M289/A319, and M289/N322) show peptide fragments (higher MW)
1006 sensitive to the reducing agent and indicate disulfide bond formation (indicated by arrow). A
1007 cystine pair (N285/G329) predicted to be far apart by the model does not result in the higher MW
1008 species.

1009

Figure 3

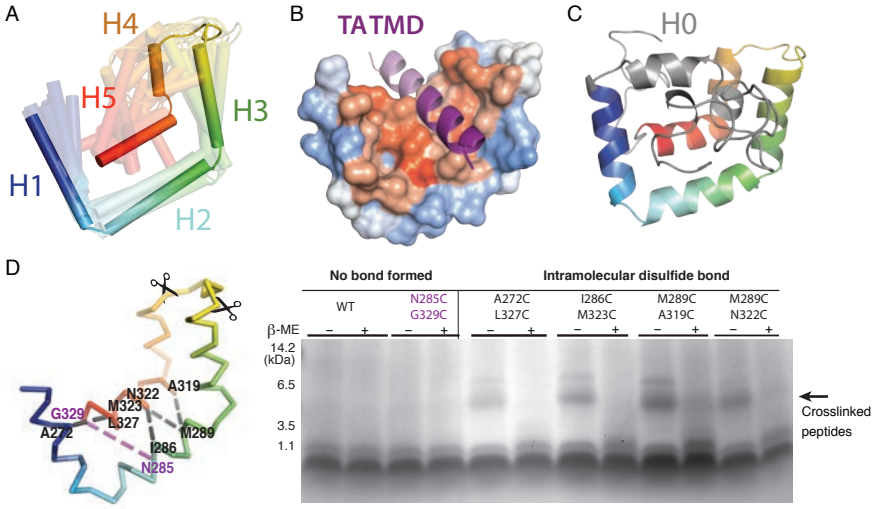
A
H4
H5
H3
H1
H2
B
TATMD
C
H0
D
G329
A272
N322
M323
L327
A319
M289
I286
N285
No bond formed
Intramolecular disulfide bond
WT
N285C
G329C
A272C
L327C
I286C
M323C
M289C
A319C
M289C
N322C
β-ME
14.2
(kDa)
6.5
3.5
1.1
Crosslinked
peptides

1011 **Fig. 4. Comparison of STI1 domains and the Sgt2-C_{cons} model.** (*A*) Multiple sequence alignment
1012 of Sgt2-C with STI1 domains (DP1, DP2) from STI1/Hop homologs. Helices are shown based on
1013 the Sgt2-C_{cons} model and the *Sc*Sti1-DP1/2 structures. Species for representative sequences are
1014 from *S. cerevisiae (Scer)*, *S. pombe* (*Spom*), *C. thermophilum* (*Cthe*), *C. savignyi* (*Csav*), and *H.*
1015 *sapiens* (*Hsap*). (*B*) Cα ribbon of *Sc*Sgt2-C_{cons} color-ramped with large hydrophobic sidechains
1016 shown as grey sticks (sulfurs in yellow). (*C*) Similar to *B* for the solution NMR structure of Sti1-
1017 $DP2_{526-582}$ (PDBID: 2LLW) [55]. (*D*) Superposition of the Sgt2-C_{cons} (blue) and Sti1-$DP2_{526-582}$
1018 (red) drawn as cartoons.

1019

Figure 4

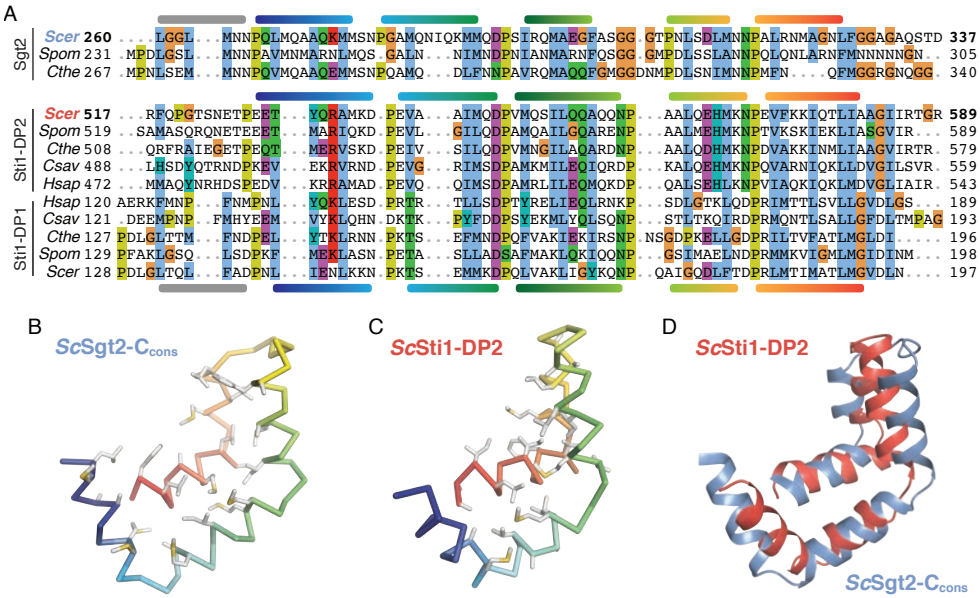
A
Sgt2
Scer 260 ...LGGL...MNNPQLMQAAQKMMSNPGAMQNIQKMMQDPSIRQMAEGFASGG.GTPNLSDLMNNPALRNMAGNLFGGAGAQSTD 337
Spom 231 .MPDLGSL...MNNPAVMNMARNLMQS.GALN...NIMNDPNIANMARNFQSGG.GMPDLSSLANNPQLQNLARNFMNNNNNGN.. 305
Cthe 267 .MPNLSEM...MNNPQVMQAAQEMMSNPQAMQ...DLFNNPAVRQMAQQFGMGGDNMPDLSNIMNNPMFN....QFMGGRGNQGG. 340
Sti1-DP2
Scer 517 ...RFQPGTSNETPEET...YQRAMKD.PEVA...AIMQDPVMQSILQQAQQNP...AALQEHMKNPEVFKKIQTLIAAGIIRTGR 589
Spom 519 ..SAMASQRQNETEEET...MARIQKD.PEVL...GILQDPAMQAILGQARENP...AALMEHMKNPTVKSKIEKLIASGVIR... 589
Cthe 508 ...QRFRAIEGETPEQT...MERVSKD.PEIV...SILQDPVMNGILAQARDNP...AALQDHMKNPDVAKKINMLIAAGVIRTR. 579
Csav 488 ...LHSDYQTRNDPKEV...EKRVRND.PEVG...RIMSDPAMKMILEQIQRDP...KALQEHMKNPQVARNIQKLLDVGILSVR. 559
Hsap 472 ...MMAQYNRHDSPEDV...KRRAMAD.PEVQ...QIMSDPAMRLILEQMQKDP...QALSEHLKNPVIAQKIQKLMDVGLIAIR. 543
Sti1-DP1
Hsap 120 AERKFMNP...FNMPNL...YQKLESD.PRTR...TLLSDPTYRELIEQLRNKP...SDLGTKLQDPRIMTTLSVLLGVDLGS... 189
Csav 121 .DEEMPNP..FMHYEEM...VYKLQHN.DKTK...PYFDDPSYEKMLYQLSQNP...STLTKQIRDPRMQNTLSALLGFDLTMPAG 193
Cthe 127 PDLGLTTM...FNDPEL...YTKLRNN.PKTS...EFMNDPQFVAKIEKIRSNP.NSGDPKELLGDPRILTVFATLMGLDI..... 196
Spom 129 PFAKLGSQ...LSDPKF...MEKLASN.PETA...SLLADSAFMAKLQKIQQNP...GSIMAELNDPRMMKVIGMLMGIDINM... 198
Scer 128 PDLGLTQL...FADPNL...IENLKKN.PKTS...EMMKDPQLVAKLIGYKQNP..QAIGQDLFTDPRLMTIMATLMGVDLN.... 197
B
ScSgt2-Ccons
C
ScSti1-DP2
D
ScSti1-DP2
ScSgt2-Ccons

1021 **Fig. 5. Effects on TA client binding of charge mutations to the putative hydrophobic groove**
1022 **of Sgt2/A-C$_{cons}$.** For these experiments, individual point mutations are introduced into Sgt2/A-C
1023 and tested for their ability to capture Sbh1 quantified as in Figure 2*D*. (*A*) For *Sc*Sgt2-C, a
1024 schematic and cartoon model are provided highlighting the helices and sites of individual point
1025 mutants both color-ramped for direct comparison. For the cartoon, the docked TMD is shown in
1026 purple. Binding of MBP-tagged Sbh1 to His-tagged *Sc*Sgt2-C and mutants were examined as in
1027 Figure 2*D*. Lanes for mutated residues are labeled in the same color as the schematic *(B)* Same
1028 analysis as in *A* for *Hs*SGTA-C. In addition, double point mutants are included.

1029

Figure 5

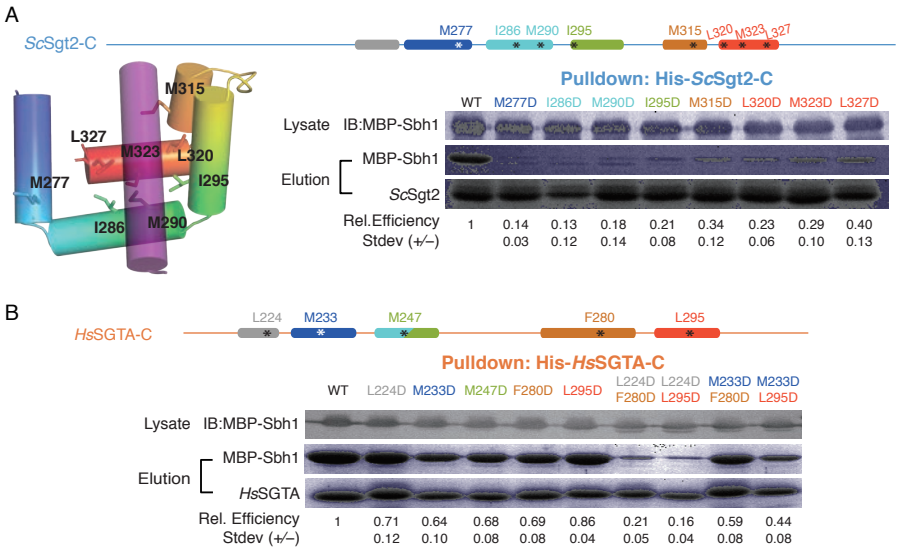
A
ScSgt2-C
M277
I286
M290
I295
M315
L320
M323
L327
M315
L327
M323
L320
M277
I295
I286
M290
Pulldown: His-ScSgt2-C
WT
M277D
I286D
M290D
I295D
M315D
L320D
M323D
L327D
Lysate
IB:MBP-Sbh1
Elution
MBP-Sbh1
ScSgt2
Rel.Efficiency
Stdev (+/–)
1
0.14
0.03
0.13
0.12
0.18
0.14
0.21
0.08
0.34
0.12
0.23
0.06
0.29
0.10
0.40
0.13
B
HsSGTA-C
L224
M233
M247
F280
L295
Pulldown: His-HsSGTA-C
WT
L224D
M233D
M247D
F280D
L295D
L224D F280D
L224D L295D
M233D F280D
M233D L295D
Lysate
IB:MBP-Sbh1
Elution
MBP-Sbh1
HsSGTA
Rel. Efficiency
Stdev (+/–)
1
0.71
0.12
0.64
0.10
0.68
0.08
0.69
0.08
0.86
0.04
0.21
0.05
0.16
0.04
0.59
0.08
0.44
0.08

1031 **Fig. 6. Minimal requirements for client recognition by Sgt2/A.** (*A*) Schematic of model TA
1032 clients. Quantification of complex formation is calculated and normalized to that of complexes
1033 containing a WT natural TA, here defined as relative binding efficiency. For this figure the WT
1034 protein is Bos1. (*B*) Complex formation of *Sc*Sgt2 (blue) and *Hs*SGTA (orange) with the TA Bos1
1035 and several artificial TAs noted x[Ly], where x denotes the length of the TMD and y denotes the
1036 number of leucines in the TMD. The helical wheel diagrams of TAs here and for subsequent panels
1037 with leucines colored in dark orange, alanines colored in pale orange, and tryptophans colored in
1038 grey. (*C*) Complex formation of *Sc*Sgt2 TPR-C and *Hs*SGTA TPR-C with artificial TA IMPs with
1039 TMDs of length 11 and increasing numbers of leucine. (*D*) Comparison of complex formation of
1040 *Sc*Sgt2 TPR-C and *Hs*SGTA TPR-C with artificial TA IMPs of the same lengths and
1041 hydrophobicities but differences in the distribution of leucines, i.e. clustered (solid line) vs
1042 distributed (dotted line).

1043

Figure 6

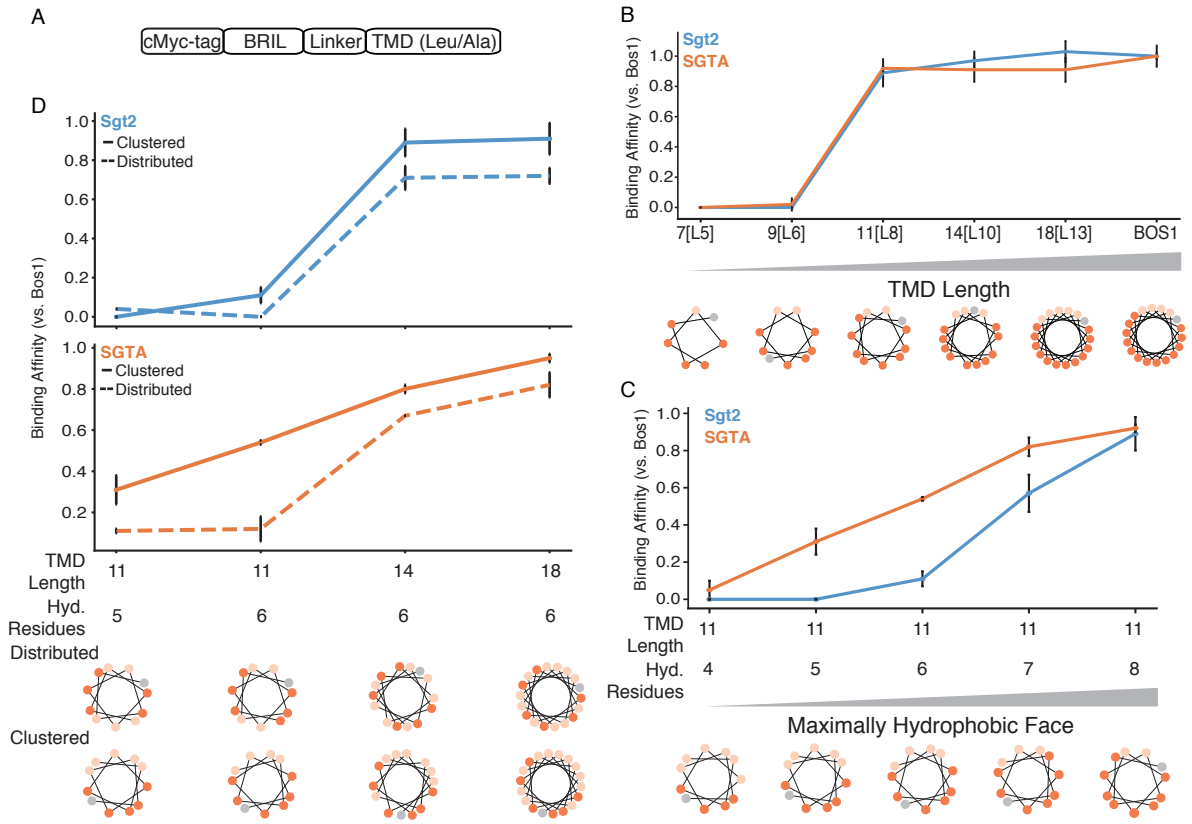
A
cMyc-tag
BRIL
Linker
TMD (Leu/Ala)
D
Sgt2
Clustered
Distributed
SGTA
Clustered
Distributed
Binding Affinity (vs. Bos1)
TMD Length
Hyd. Residues
Distributed
Clustered
B
Sgt2
SGTA
Binding Affinity (vs. Bos1)
7[L5]
9[L6]
11[L8]
14[L10]
18[L13]
BOS1
TMD Length
C
Sgt2
SGTA
Binding Affinity (vs. Bos1)
TMD Length
Hyd. Residues
Maximally Hydrophobic Face

1045 **Fig. 7. Hydrophobic properties and localization of natural TA IMPs.** (*A*) A summary of
1046 putative yeast and human TA IMPs by their experimentally validated localization [60]. Using the
1047 definition of a single TMD within 30 residues of their C-terminus gives the final numbers of 90
1048 for yeast and 587 for humans. (*B*) A plot of all predicted yeast TA IMPs comparing two separate
1049 metrics for measuring the hydrophobicity of their TMD, either the entire TMD or the most
1050 hydrophobic helical face. Each protein is represented by an open circle colored based on
1051 localization including those with both mitochondrial and ER localization. Additionally, proteins
1052 with ER or mitochondrial localizations are highlighted on each axis. Proteins noted in the text are
1053 highlighted. The best cut-offs for predicting mitochondrial versus ER for either metric are
1054 represented by dotted lines (dark red, TMD hydrophobicity of entire TMD; light blue: TMD
1055 hydrophobicity of the most hydrophobic face). (*C*) As in *B* for putative human TA IMPs. (*D*)
1056 Quantitative comparison of the effectiveness of each metric by either the number of correctly
1057 predicted ER and mitochondria TA IMPs and the area under a ROC curve (AUROC).

1058

Figure 7

A

	S. cerevisiae	*H. sapiens*
ER	35	117
Mitochondria	5	27
Both	1	10
Peroxisome	1	4
Unknown	46	418
Total	90	576

C

	S. cerevisiae		*H. sapiens*	
	Overall	Face	Overall	Face
Correctly Predicted ER + Mito **(%)**	32 (80)	38 (95)	96 (67)	104 (72)
AUROC	0.87	0.99	0.79	0.82

B

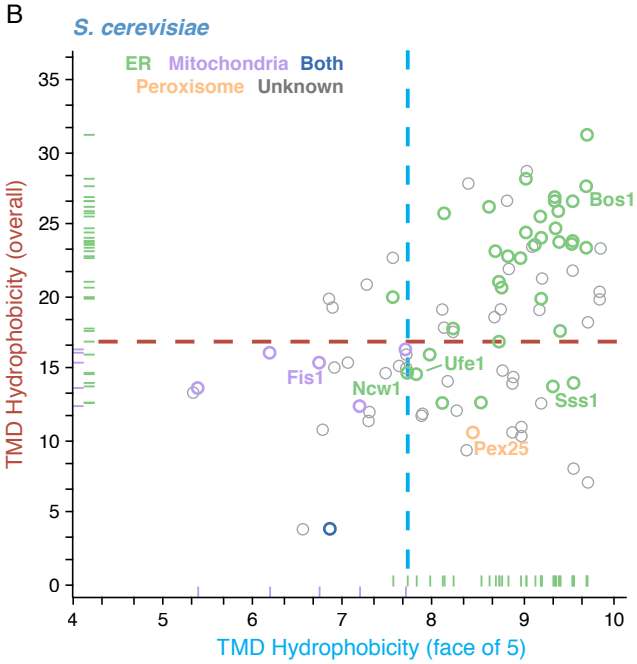

D

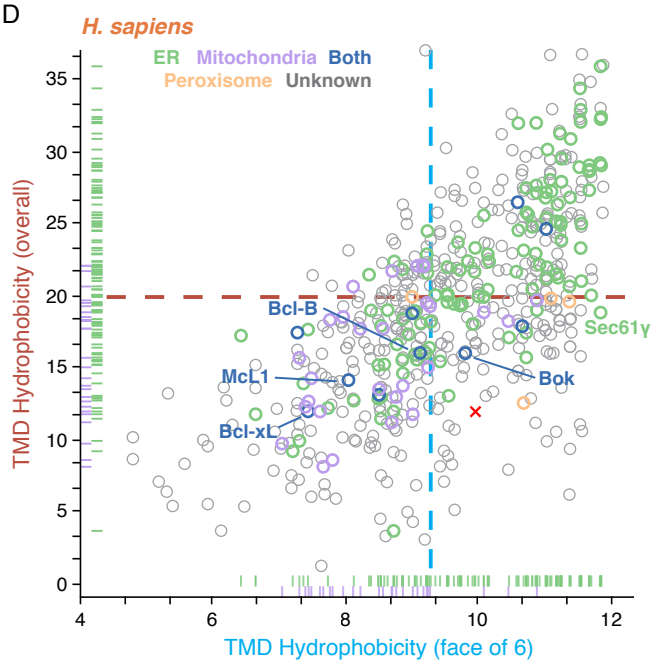

1060 **Fig. 8. Various domain structures of STI1 and other helical-hand containing proteins.** (*A*)
1061 The domain architectures of proteins with a STI1 domain were obtained initially from InterPro
1062 [60] and then adjusted as discussed in the text. Each domain within a protein is colored relative to
1063 the key. (B) Structural comparison of various hydrophobic-binding helical-hand protein
1064 complexes. For each figure only relevant domains are included. Upper row, color-ramped cartoon
1065 representation with bound helices in purple. Lower row, accessible surface of each protein colored
1066 by hydrophobicity again with docked helical clients in purple. In order, the predicted complex of
1067 *Sc*Sgt2-C_{cons} and *Sc*Sbh2-TMD, DP1 domain from yeast Sti1 with N-terminus containing H0 in
1068 grey (*Sc*Sti1-DP1)(PDBID: 2LLV), STI1 domain from yeast Rad23 (*Sc*Rad23-STI1) bound to the
1069 TMD of RAD4 (*Sc*RAD4-TMD) (PDBID: 2QSF), human calmodulin (*Hs*CALM2) bound to a
1070 hydrophobic domain of calcineurin (*Hs*PPP3CA) (PDBID: 2JZI), and M domain of SRP54 from
1071 *Oryctolagus cuniculus* (*Oc*SRP54-M) and the signal sequence of human transferrin receptor
1072 (*Hs*TR-TMD) (PDBID: 3JAJ).

1073

Figure 8

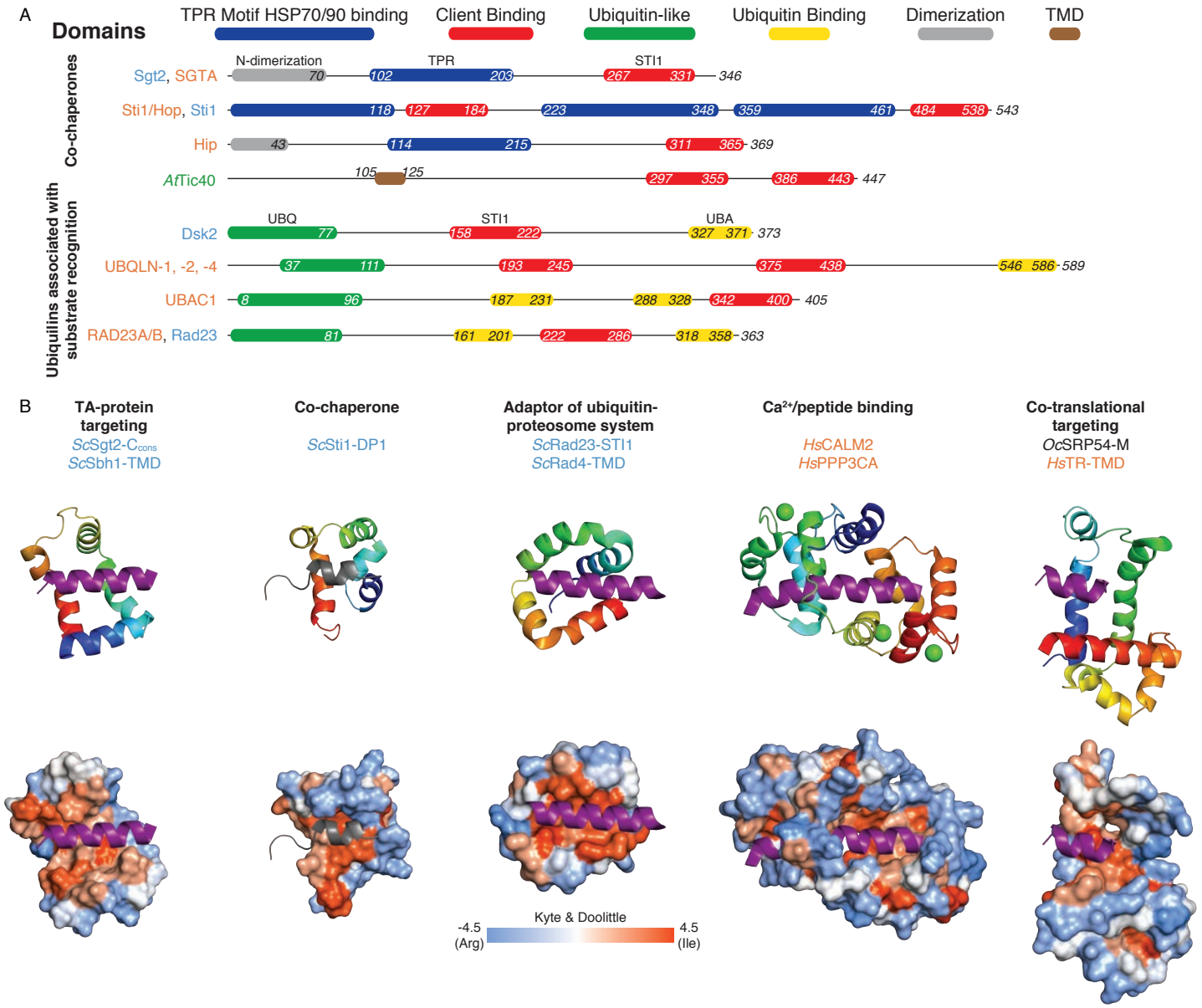
A
Domains
TPR Motif HSP70/90 binding
Client Binding
Ubiquitin-like
Ubiquitin Binding
Dimerization
TMD
Co-chaperones
Ubiquilins associated with substrate recognition
Sgt2, SGTA
N-dimerization
TPR
STI1
Sti1/Hop, Sti1
Hip
AfTic40
Dsk2
UBQ
STI1
UBA
UBQLN-1, -2, -4
UBAC1
RAD23A/B, Rad23
B
TA-protein targeting
ScSgt2-Ccons
ScSbh1-TMD
Co-chaperone
ScSti1-DP1
Adaptor of ubiquitin-proteosome system
ScRad23-STI1
ScRad4-TMD
Ca2+/peptide binding
HsCALM2
HsPPP3CA
Co-translational targeting
OcSRP54-M
HsTR-TMD
Kyte & Doolittle
-4.5 (Arg)
4.5 (Ile)

1075 **Fig. S1. Biophysical characterization of the Sgt2/A-C_{cons} domain.** (*A*) CD spectra as in Fig. 1*C*
1076 for the conserved C-terminal domains of Sgt2 (blue) and SGTA (orange). (*B*) NMR spectra as in
1077 Fig. 1*D* & *E* for Sgt2-C_{cons} (blue) and SGTA-C_{cons} (orange).

1078

Figure S1

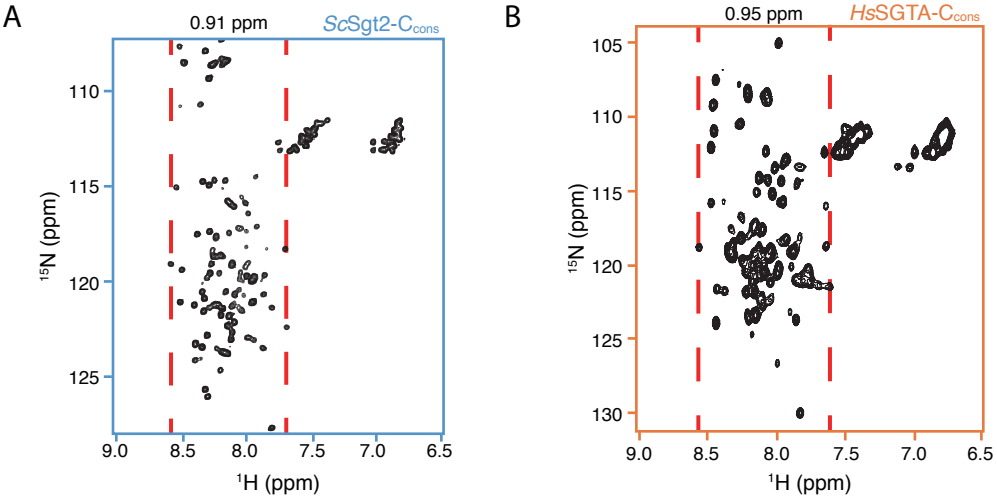
A
0.91 ppm
ScSgt2-Ccons
110
115
120
125
15N (ppm)
9.0
8.5
8.0
7.5
7.0
6.5
1H (ppm)
B
0.95 ppm
HsSGTA-Ccons
105
110
115
120
125
130
15N (ppm)
9.0
8.5
8.0
7.5
7.0
6.5
1H (ppm)

1080 **Fig. S2. Characterization of STI1 domains.** Predicted [117] and calculated [118] secondary
1081 structure elements (*A*) and a structure-based alignment (*B*) of STI1 domains from Fig. 8*A* in the
1082 ClustalX color scheme [119]. Dashed lines in *A* depict previous domain boundary annotations. (*C*)
1083 Helical wheel diagrams of H0 of STI1 domains. (*D*) Additional STI1 domain structures
1084 represented as in Fig. 8*B*. Domains are from the DP2 domain from yeast Sti1 (*Sc*Sti1-DP2)
1085 (PDBID:2LLW), the chloroplast import protein Tic40 from *Arabidopsis thaliana* (*At*Tic40-STI1)
1086 (PDBID:2LNM), and yeast Rad23 (*Sc*Rad23-STI1) bound to the N-terminus of PNGase
1087 (*Sc*PNGase-N-term) (PDBID: 1X3W).

1088

Figure S2

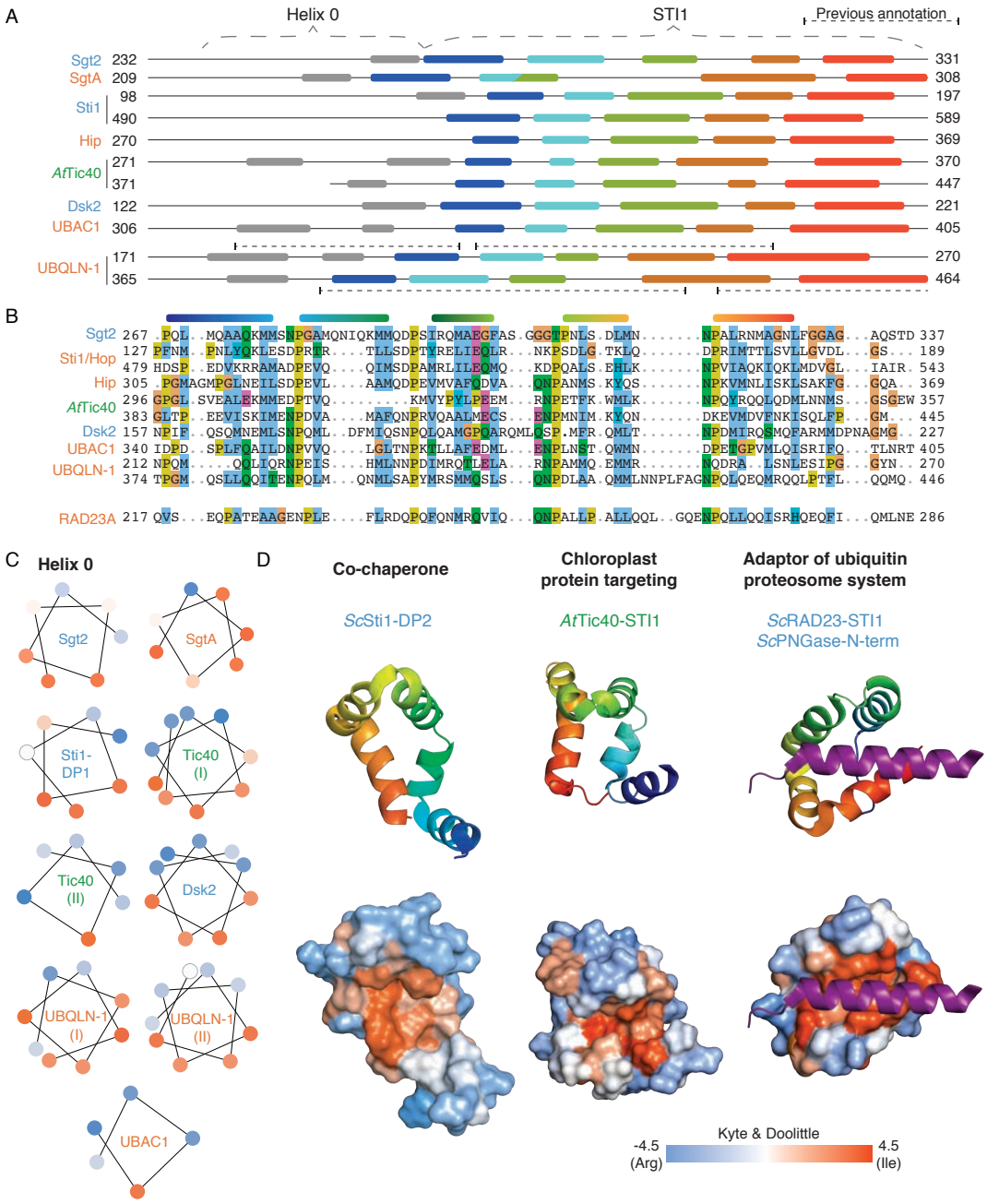
A
Helix 0
STI1
Previous annotation
Sgt2 232 331
SgtA 209 308
Sti1 98 197
490 589
Hip 270 369
AtTic40 271 370
371 447
Dsk2 122 221
UBAC1 306 405
UBQLN-1 171 270
365 464
B
Sgt2
Sti1/Hop
Hip
AtTic40
Dsk2
UBAC1
UBQLN-1
RAD23A
C
Helix 0
Sgt2
SgtA
Sti1-DP1
Tic40 (I)
Tic40 (II)
Dsk2
UBQLN-1 (I)
UBQLN-1 (II)
UBAC1
D
Co-chaperone
ScSti1-DP2
Chloroplast protein targeting
AtTic40-STI1
Adaptor of ubiquitin proteosome system
ScRAD23-STI1
ScPNGase-N-term
Kyte & Doolittle
-4.5 (Arg)
4.5 (Ile)

1090 **Table S1. TA Database.** A compilation of the putative yeast (Sheet 1) and human (Sheet 2) TA
1091 proteins shown in Fig. 7*B*,*C*. The Uniprot identifiers, predicted TMD sequence and prediction
1092 method, subcellular localization string and resulting inferred target localization, and
1093 hydrophobicity metrics (face and overall) are listed for each protein. Those labeled on the plot or
1094 mentioned in the text are highlighted along with the abbreviations used. (Sheet 3) A comparison
1095 with yeast TA proteins previously compiled by [64] with an explanation of differences, where they
1096 exist.

1097